Title

Solving the Mysteries of Novel Cytoskeletal Assemblages through Cryo-EM

ISBN

9798190900033

Author

Nie, Chuankai

Publication Date

2026-09-03

Peer reviewed|Thesis/dissertation

Solving the Mysteries of Novel Cytoskeletal Assemblages through Cryo-EM

by
Chuankai Nie

DISSERTATION
Submitted in partial satisfaction of the requirements for degree of
DOCTOR OF PHILOSOPHY

in

Biophysics

in the

GRADUATE DIVISION
of the
UNIVERSITY OF CALIFORNIA, SAN FRANCISCO

Approved:

DocuSigned by:
Dyche Mullins
E4FB70A20A7546F...

Dyche Mullins
Chair

DocuSigned by:
Yifan Cheng
DocuSigned by:

Yifan Cheng

Sophie Dumont
8305715E0D454DC...

Sophie Dumont

Committee Members

Acknowledgements

It is no easy task to navigate the edge of a field of science through the course of a PhD candidacy. I am eternally thankful for the support network of my friends, family, colleagues, and mentors during this portion of my life and education.

Firstly, I cannot overstate my gratitude to Dyche Mullins, the supreme leader of our group, for not only building a lab where fascinating ideas come to be explored, but also for nurturing and enabling a positively jovial environment where we comrades of science have gathered. As an all-around wizard of cell-biology and cytoskeletal dynamics, it was always fascinating to watch him piece together stories from a variety of organisms to help answer our own scientific questions. On top of that, he possesses a strong literacy for media and an instinct for philosophy that make any casual discussions of contemporary books, movies, or ideas just plain fun. Through my project's setbacks and dead-ends, he has always continued to support me, in morale and otherwise. The Mullins Lab is filled with wonderful, beautiful people pursuing wonderful, beautiful work. I wouldn't have been able to get my feet on the ground of these projects if it wasn't for the mentorship of Natalie Petek-Seoane. Her excitement and enthusiasm for the structural discoveries of the cytoskeletons we both loved to study always lit up my day. I also wanted to thank my collaborators within the lab for bringing their intriguing systems to my realm of structure: Arthur Charles-Orzsag, Arghya Bhowmick, and Justin Salat. I don't think I've yet met a young investigator as talented and knowledgeable as Arthur in his field of archaeal studies. I wish him the best in his endeavors as he unlocks the questions of what are perhaps the most existentially, philosophically important questions surrounding how life as we know it evolved.

In addition, I wanted to extend my thanks to the members of my thesis committee, Sophie Dumont and Yifan Cheng. This work required a strong understanding of the technical aspects of cryo-EM but critically, it demanded a grounding in the biologies of the systems being studied. The discussions we've had within and without our regular meetings helped me shape both of these principles throughout the course of my thesis, and for that I am grateful for their insights.

I am eternally indebted to David Bulkley and Glenn Gilbert of the UCSF EM Core for their tutelage. They trained me in the techniques of cryo-EM sample preparation and data collection and were always patient and helpful whenever I had questions about EM or concerns about the flashing lights on the microscope. I am always delighted to work with both of them.

Once the data was collected, I of course had to learn how to process it. For this I am thankful to Justin Kollman and Anika Burrell from my undergraduate lab and Bryan Faust who were all formative to my early cryo-EM education. I also credit Hao Wu for his practical advice and guidance on model-building.

I am grateful to my friends in the Biophysics program at UCSF: Rian, Andrew A., Dom, Maxine, Garrison, and Ashley. Alongside our "COVID Cohort", we really did make the best of things and had a good time doing it. I hope one day, though, I can defeat Maxine in a game of tennis (one can dream).

For starting me on my path to studying biology and biochemistry, I wanted to thank my high school biology teacher Mr. Briggs and my brother Johnny for their inspiration and advice.

I would certainly not be here without the upbringing that my family provided me. I am deeply beholden to my father, mother, and brother for their encouragement, discipline, and love. I still believe I have a lot to live up to when it comes to these amazing people.

I wanted to thank my dear friends Andrew B., Abraham, Sean, Charrley, Jared, and Daniel for being the devoted DnD players of the campaign I have been running for three years. May we continue to have the best of adventures and may you eventually understand that "the shards are not and never were weapons".

Finally, I wanted to profess my appreciation for my fiancé and the love of my life, Linda. She has made a better man out of me and we've only continued to become a stronger team over the years. Her constant support and lovely company have eased the burdens of this endeavor and I can't imagine any obstacle we can't overcome. I am so excited for the bright future that awaits us and the new stories we get to experience. Let's make it a good one, I love you.

Contributions

Chapter 1

Figures 1.1, 1.2, 1.3, and 1.4 were prepared by Chuankai Nie for the S2Actin and Tm1J/2A heterodimer manuscripts.

Chapter 2

Protein purification, biochemical validation, UV crosslinking, and DNA constructs were performed by Justin Salat. Cryo and negative stain electron microscopy were performed by Chuankai Nie.

Figure 2.1 was produced by Justin Salat as part of the Arp2/3 DNA binding manuscript. Figures 2.2, 2.3, 2.4, 2.5, and 2.6 were produced by Chuankai Nie.

The discussion section was written by Chuankai Nie as a draft for the Arp2/3 binding manuscript.

Chapter 3

Alp7A protein purification and sample preparation was performed by Natalie A. Petek-Seoane. SegA protein purification and sample preparation was performed by Arghya Bhowmick and Arthur C. Orzsag. TA0583 protein purification and sample preparation was performed by Arghya Bhowmick. Cryo-EM was performed by Chuankai Nie.

Solving the Mysteries of Novel Cytoskeletal Assemblages through Cryo-EM

Chuankai Nie

Abstract

Actin is a supremely conserved cytoskeletal protein whose homologs can be found across eukaryotes, archaea, and bacteria. Polymerized into micrometer-scale filaments, actin networks organize within the cell to accomplish several critical functions such as motility, division, and mechanosensing. To perform these functions, the actin cytoskeleton must adopt a variety of morphologies with spatial precision, which is all controlled by a vast menagerie of actin-regulating proteins. The Mullins Lab is broadly interested in delineating the structure-function relationships of these proteins in the context of cellular and molecular biology. A key tool for studying the structure and function of actin and actin-regulators is cryo-electron microscopy (cryo-EM), which enables near-atomic resolution visualization of *in vitro* and *in vivo* systems of proteins in hydrated environments. In this dissertation, we will explore the unique insights gained into several actin cytoskeleton systems through single particle cryo-EM, a result of years of collaborative work with the talented cell biologists and biochemists within the lab. In Chapter 1, I characterize the binding posture of novel *Drosophila* tropomyosins on actin filaments, present the world's first fly actin polymer structure, and report my attempts to engineer a fiducial onto tropomyosin. In Chapter 2, I elucidate the binding sites of single-stranded DNA to the Arp2/3 complex which compete with the VCA of nucleation promoting factors. In Chapter 3, I present my work in investigating the cytoskeletal elements of non-eukaryotic organisms: SegA from Sulfolobus, Alp7A from Bacillus subtilis, and Ta0583 from Thermoplasma acidophilum.

Table of Contents

List of Figures

List of Tables

Chapter 1: Helical Tropomyosin Structures from Drosophila and Human, and the Search for Fiducials to Elucidate the Tropomyosin Junction

Introduction

Actin is a supremely conserved, ancient protein which is found across eukaryotic and non-eukaryotic forms of life (Charles-Orzsag et al., 2024; Derman et al., 2009; Muller et al., 2005) Monomers of actin can polymerize into two-start helical filaments which then assemble into complex 3D networks of diverse morphologies to perform numerous critical cellular functions. Such functions include cell motility (Pollard & Borisy, 2003), mechanosensing (Hayakawa et al., 2012), division (Pollard, 2008) , and transcription (Chen & Shen, 2007). To achieve this diverse portfolio of actin structures and functions, actin is accompanied by a vast menagerie of regulators which carefully interplay within the cell to control the localization and architecture of actin. Analogous to how varied genetic expression is a determinant of cell differentiation, a cohort of actin-regulating proteins affixed to an actin network locally differentiates the actin's function. Chief among these regulators are the tropomyosins, a family of proteins which are understood to regulate nearly all actin cytoskeleton functions (Gunning et al., 2008).

Tropomyosin (Tm) is the quintessential alpha-helical coiled coil dimer. In humans, four tropomyosin genes encode upwards of 40 isoforms through RNA splicing, with cells expressing around 6-7 isoforms depending on differentiation (Gunning et al., 2008). Tropomyosins regulate actin by binding to actin filaments in a lengthwise fashion and, critically, associating with neighboring tropomyosin dimers in what is known as a four-helix junction. Junctioning of multiple tropomyosins creates a continuous polymer of tropomyosin along both broad faces of the actin filament which can be referred to as a copolymer (Huxley, 1973). Fascinatingly, although canonical tropomyosin isoforms adopt the same lengthy coiled-coil morphology and possess high sequence similarity, tropomyosins are highly specialized and non-redundant in

regulatory function. For example, Tm 3.1 has been shown to be highly protective against actin filament severing via cofilin while Tm 2.1 exhibits no such protective activity (Gateva et al., 2017; Jansen and Goode, 2019), and Tm 4.2-coated filaments stimulate myosin IIa binding whereas Tm 1.6/1.7 does not (Gateva et al., 2017). Dysregulation of different tropomyosin isoforms has been implicated in multiple human diseases (Xu, T. et al., 2024; Ly et al., 2018; Zhu et al., 2025), making them not only of interest from a basic scientific perspective but also a potential area for therapeutic investigation.

Scheider 2 (S2) cells, a drosophila-derived macrophage-like cell line, express only three isoforms of tropomyosin from two genes: Tm1A, Tm1J, and Tm2A. Prior work in the lab illuminated the distinct and novel cellular localizations of these isoforms (Goins and Mullins, 2015), motivating a biochemical survey. Further assaying work by Jenny Hsiao and Johnny Rodriguez in our lab revealed several surprising idiosyncrasies of these tropomyosins. Firstly, Tm1A was rejected from binding to Acanthamoeba actin which is bizarre due to the high sequence and structural identity of all eukaryotic actins which should permit interaction with actin-targeting proteins. And secondly, Tm1J and Tm2A were unable to bind any actins whatsoever, but actin binding activity was "restored" when Tm1J/2A assembled into a coiled-coil heterodimer (unpublished)- an unprecedented behavior in tropomyosins thus far. Unraveling the molecular interactions which drive these novel behaviors would generate new insights into how tropomyosins can assemble to regulate actin, and the ideal tool to interrogate the structure of tropomyosin bound to actin is cryo-electron microscopy (cryo-EM).

Single particle cryo-EM has been utilized with great success to unravel the 3D-organization of actin assemblages at near-atomic resolutions (Oosterheert et al., 2022; Risi et al., 2022; Yamada et al., 2020). Although tropomyosins possess a simple fold with high stability

when bound to actin, and structural investigations of tropomyosin have been successful using X-Ray crystallography on fragments of tropomyosin (Rao et al., 2012), acquiring a high resolution cryo-EM structure of this protein is frustrated by several factors. The first obvious issue is a difference in helical symmetry between actin and tropomyosin: although tropomyosin can stably saturate actin such that they form a homogenous copolymer, Tms cover six to seven monomers of actin. This periodicity mismatch results in the smearing of the tropomyosin's signal and forces us to use single particle means to properly resolve the tropomyosin. Another problem is that the electron density of tropomyosin's four-helix junction is not prominent (constituting approximately 5.5kDa of protein) thus posing an issue of having low signal-to-noise, especially in comparison to the "noise" of the actin filament. To improve our resolution of cryo-EM structures of tropomyosin on actin, we will use biochemical tricks to address these challenges.

In Chapter 1, I present my work on characterizing the 3D-structure of Drosophila tropomyosin and tropomyosins 1A, 1J, and 2A from Drosophila cells using cryo-EM. Using a Tm-targeting drug I also show that a sufficient disruption to the symmetry of the tropomyosin polymer can allow for some selection of particle classes for a low-res reconstruction of the tropomyosin junction.

Results

Cryo-EM Reconstruction of Drosophila Actin

We began our investigation by first natively purifying Drosophila actin from S2 cells using a previously established protocol. Briefly: Schneider 2 cells were lysed and mixed with recombinantly purified Gelsolin 4-6 in order to capture native actin. Despite the importance of Drosophila as a model system for muscle twitching and flight muscles (processes necessitating actin networks), there exists no high-resolution cryo-EM structure of its actin filament. Using helical refinement, we were able to reconstruct a 2.8A structure of the S2 actin filament (Figure 1.1). Our cryo-EM structure revealed a S2 actin's helical parameters are in alignment with well-characterized mammalian actins: possessing a helical twist of -166.5° and a rise of 27.4 Å. Comparing the structure of the filament- incorporated monomer to rabbit skeletal actin, we found that the monomers have an all-backbone RMSD of 0.390A (Figure 1.1). Given that this Drosophila actin was purified natively from S2 cells, we wanted to know which isoform was predominantly represented by the structure. Drosophila melanogaster expresses six isoforms of actin depending on cell differentiation (Röper et al., 2005), by interrogating the side chains of our actin structure where they are diverged revealed that Drosophila actin 5C was the primary form in our sample (Figure 1.2). This finding is also consistent with mass-spectrometry analysis previously done in the lab on S2 actin (unpublished).

Both Drosophila Tms 1A and 1J/2A Adopt C-State Positions Along the Actin Filament

To understand the mechanisms driving tropomyosin species specificity (Tm1A) and heterodimerization (Tm1J/2A), we sought the structure of these Tms bound to actin. Rabbit skeletal actin filaments were prepared through a native preparation of rabbit muscle acetone powder; Drosophila actin was natively purified from S2 Cells. Tropomyosins were all

recombinantly purified from *E. coli*, and possess an Alanine-Serine insertion at the N-terminus to mimic N-terminal acetylation (Monteiro et al., 1994). We resolved several helically-refined structures of tropomyosin in complex with actin: Tm1a with S2 actin and with rabbit actin, Tm1J/2A with S2 actin, and Tm3.1 (a human tropomyosin) with rabbit actin (Figure 1.3-1.5)(Table 1). Using helical reconstruction, our actin filaments were resolved to resolutions around 3A, but the tropomyosins were smeared and poorly resolved. Loss of tropomyosin information is largely due to the heterogeneity of the pair of tropomyosin's longitudinal position along the filament and the difference in helical symmetry between tropomyosin and actin. All Drosophila tropomyosins bound to actin in the normative C-state, which, in the skeletal context is the myosin-ready state (Figure 1.4).

Fiducial Strategies to Increase the Molecular Weight of the Tm Junction

To reconstruct tropomyosin at a higher resolution, we decided to mimic a single particle strategy that had been demonstrated to work for natively purified thin filaments (Risi et al., 2022). The concept was as follows: using electron-dense fiducials which were attached to tropomyosin in such a way that particles selected with the fiducial present would be homogenous in terms of tropomyosin-pair posture (or, at the very least, break the symmetry of the actin-tropomyosin complex enough for particle sorting). Importantly, we aimed for a method that would be applicable to any tropomyosin isoform (Figure 1.6). An important addition to our sample preparations was tropomodulin, which is a tropomyosin nucleator at the pointed end of actin. Normally, tropomyosins will randomly bind actin along its length. This high heterogeneity of "start points" for the tropomyosin cable on both filament faces is inconvenient for cryo-EM data quality. By using tropomodulin we enforce the nucleation of tropomyosin cables on actin and thus homogenize the position of the tropomyosin with respect to the tropomyosin on the

opposite face of the filament. We then experimented with multiple methods to add such a fiducial to the tropomyosin: direct binding with anti-Tm antibodies, biotinylating tropomyosin to bind streptavidin, and N-terminal fluorescent protein fusions (Figure 1.7). Relying on tropomyosin cross-reactivity, we tested several purchasable anti-TM antibodies (F-6 and C-3, Santa Cruz Bio; D5A7, Cell Signaling Technology) but none of them were found to bind our Drosophila tropomyosins (not shown). We were able to reconstitute complexes of tropomyosin-actin with attached streptavidin or fluorescent protein, and these fiducials were visible in 2D class averages from cryo-EM, but none of these particles yielded a high resolution structure of tropomyosin (or its junction)(Figure 1.7-1.8). We more deeply discuss the strategy, generation, and failure of these fiducials in the succeeding Discussion and Methods sections.

C-Terminal-targeting Drug ATM3507 Induces a Symmetry Break in the Tm Polymer

ATM3507 is a small molecule drug which targets the C-terminus of Tropomyosin 3.1 and embeds itself within the 4-helix junction (Currier et al., 2017)(Figure 1.9). Given its intrusion and disruptive effect on tropomyosins bound to actin, we sought to use it not as a fiducial per se (given its small molecular weight), but to "bulge out" the tropomyosin strand at the junctions where the drug binds, potentially enabling particle classification. Interestingly, our helically-refined structure of Tm3.1 in the presence of ATM3507 indeed shows a discrepancy in the continuous coiled-coil which wraps around the actin filament. This small, but prominent "bump" in the density of the tropomyosin (which does not exist in the structure without ATM3507 nor other tropomyosin structures) appears at every half turn of the tropomyosin- a convolution of the bulging feature due to helical refinement (Figure 1.9). We performed 3D classification on these particles using a Tm mask, and found classes where the coil appeared to be discontinuous, which could indicate the location of a junction (Figure 1.9).

Discussion

In this chapter, we present the world's first filament structure of a Drosophila actin (isoform 5C). We initially suspected that the previously reported novel behaviors of Drosophila tropomyosins could be partially explained by a divergent co-evolution with actin, but the high structural identity of the actin 5C filament with mammalian sources suggests any divergent behavior is accredited to the tropomyosins alone. Nevertheless, it is valuable to now have a filamentous actin structure from an animal that is such a common model organism.

Our investigation into the binding interaction of tropomyosin with actin revealed that the homodimer of 1A, and the heterodimer of 1J and 2A both bound actin in a normal position (C-state in the absence of any troponin). Similar to S2 actin, we had hypothesized that the unique properties of these tropomyosin coils (species specificity and obligate heterodimerization) would also manifest a unique binding posture along the filament. Instead, it appears that these tropomyosins evolved their unique properties within the constraints of their canonical relationship to actin, suggesting that their function is closely in line with known tropomyosin functions (e.g. differential gating of actin binding partners). This finding is consistent with genetic work with S2 cells wherein it was found that the localization of the tropomyosins were strongly dependent on the sequence of their troponin binding region (Goins and Mullins, 2014).

Helical reconstruction is a technique that has successfully solved many high resolution structures of actin and other helical proteins. Unfortunately, it is virtually incapable of resolving partner proteins bound to these helical structures unless their binding was well-saturated and symmetrically harmonious with the underlying helix. While tropomyosin is certainly binding our actin filaments to a saturating degree, the high homogeneity of tropomyosin coils and the low molecular weight of the junction region make resolving tropomyosin untenable through helical

refinement. Instead, we opted for a single-particle strategy inspired from a prior study with natively extracted thin filaments. These native muscle thin filaments possess troponin complex, a roughly 75kDa protein complex which specifically associates with tropomyosin at tropomyosin's C-terminus (Tripet et al., 1997; Xu, C. et al., 1999; Yamada et al., 2020). By picking particles where the troponin complex is clearly visible flanking the actin filament, you can classify segments of the filament with highly homogenous positioning of the underlying tropomyosin and thus resolve a high resolution structure of the coiled-coil. We aimed to emulate this method for our non-muscle tropomyosins through addition of fiducials which would also flank the tropomyosin/actin at specific locations with respect to the tropomyosin. We explored several methods to add electron-dense fiducials to tropomyosin with the goal of generating a method broadly tractable to any tropomyosin.

Since tropomyosins have high structural similarity which results in antibody cross-reactivity, we tried using purchased anti-Tm antibodies to test for reactivity against our tropomyosins. We tested several antibodies (Santa Cruz, Abcam), but did not detect binding to our tropomyosin using cosedimentation assays (data not shown). Another issue of purchased antibodies is their low concentration; for cryo-EM preparations we would require roughly 0.25mg/ml final concentration of antibody, making this approach expensive. We could raise antibodies against specific isoforms, but we chose not to pursue this method in favor of developing something tractable to all isoforms.

A common technique in our lab is using click chemistry to attach fluorophores to protein for microscopy. While fluorophores are too small to be useful as EM fiducials, we realized we could biotinylate our tropomyosins using the same chemistry, allowing us to couple them to streptavidin, thus providing an electron-dense fiducial which is coupled to a specific site on the

tropomyosin. We were successful at generating pure biotinylated tropomyosins which pulled down streptavidin in co-sedimentation assays. With EM, we were able to classify 2D averages of the filament where streptavidin is visualized flanking the actin filament, but the streptavidin densities were blurry suggesting flexibility. We were unable to resolve the streptavidin in any 3D reconstructions, consistent with its poor resolution at the 2D class stage. The linker length of EZ-Link™ Amine-PEG3-Biotin which was used to biotinylate our tropomyosin is around 23 angstroms, which is acceptable for light microscopy but when combined with the flexibility of the linker results in highly heterogeneous positioning of the streptavidin, annihilating its usefulness as a fiducial.

Yet another method we attempted was the N-terminal addition of a fluorescent protein to the tropomyosin. It has been well-established that N-terminal fluorescent protein fusions of this nature yielded functional tropomyosins which could incorporate onto actin filaments both in vitro and in vivo (Brooker et al., 2016; Goins et al., 2015). For our purposes, this fusion presented another avenue to add an electron-dense fiducial to tropomyosin. We successfully generated two different versions of this fusion with Tm1A: one with Cerulean3 and one with eGFP. Both constructs bound actin during cosedimentation assays and their N-terminal fluorescent protein were visible in negative stain EM. Using cryo, we were able to visualize the beta barrel of the fluorescent protein flanking the actin filament and they are also plainly present in the reconstructions, tightly fitting with the actin filament. Problematically, there is no density corresponding to the linker between the tropomyosins and the GFP, and the tropomyosin density was completely continuous (indicating no junction) in all reconstructions where the fluorescent protein was visible. This suggests at least two possibilities: that the linker between GFP and tropomyosin is too flexible to permit high-resolution reconstruction, or that the GFP is

non-specifically associated with the filament. This method could be improved by rigidifying the connection between the GFP and tropomyosin, but it remains to be tested what length and rigidity would be amenable to cryo-EM while retaining tropomyosin's ability to incorporate as a copolymer. Future work could alternatively look to completely replicate the earlier successes of native thin filament structures by using same-species troponin complexes as fiducials.

Most excitingly, we were able to observe symmetry breaks to the junctions of human Tm 3.1 using the small molecule called ATM3507. This drug was originally designed to disturb the polymerization of isoform 3.1 in tumor cells to cause eventual apoptosis. In our study we found that the addition of ATM3507 to the tropomyosin-actin complex introduced a prominent "bump" feature that had not been previously observed on helically refined tropomyosin structures. What is especially impressive is that the perturbation must be significant and consistent to be represented within the structure even after the signal smearing of the tropomyosin during helical refinement. This work provides direct structural evidence of ATM3507's incorporation into the Tm3.1's junction and reveals the potential for such drugs to improve our structural investigations into tropomyosins.

Table 1.1 Cryo-EM data collection, refinement, and validation statistics for Actin/Tm

	RbActin+ eGFP-Tm 1A	RbActin + Tm1A	S2Actin	S2Actin + Tm1A	S2Actin + Tm1J/2A	RbActin + Tm3.1	RbActin + Tm3.1+ Drug
Data collection and processing							
Magnification	45,000	54,000	165,000x	45,000	45,000	45,000	45,000
Voltage (kV)	200	200	300	200	200	200	200
Electron Exposure (e-/A^2)	64.1	64.1	60.0	64.1	64.1	64	64
Defocus Range (μM)	-1.0-2.0	-1.0-2.0	-0.8-1.5	-1.0-2.0	-1.0-2.0	-1.0-2.0	-1.0-2.0
Pixel Size (Å)	0.865	0.73	0.4135	0.865	0.865	0.865	0.865
Initial Micrographs	6,839	6,859	14,004	12,333	3,381	1,566	1,089
Final Particle Count	23,422	667,951	649,936	293,201	408,910	68,670	206,400
Map Resolution (FSC threshold 0.143)	4.32	3.21	2.76	3.51	3.79	4.35	5.0
Refinement (Phenix)							
Initial Model Used			AF-P10987	AF-P10987+ PDB:5JLF			
Model Resolution (FSC threshold 0.5)			3.0	4,0			
Map CC (Volume)			0.84	0.56			
B Factor ($Å^2$)			127.5	189.7			
Validation							
MolProbity Score			1.34	1.39			
All-Atom Clashscore			6.10	7.03			
Rotamer Outliers			0.00	0.00			
C-Beta Outliers			0.00	0.00			
Ramachandran Plot							
Favored (%)			98.93	0.00			
Allowed (%)			1.07	0.96			
Outliers (%)			0.00	99.04			

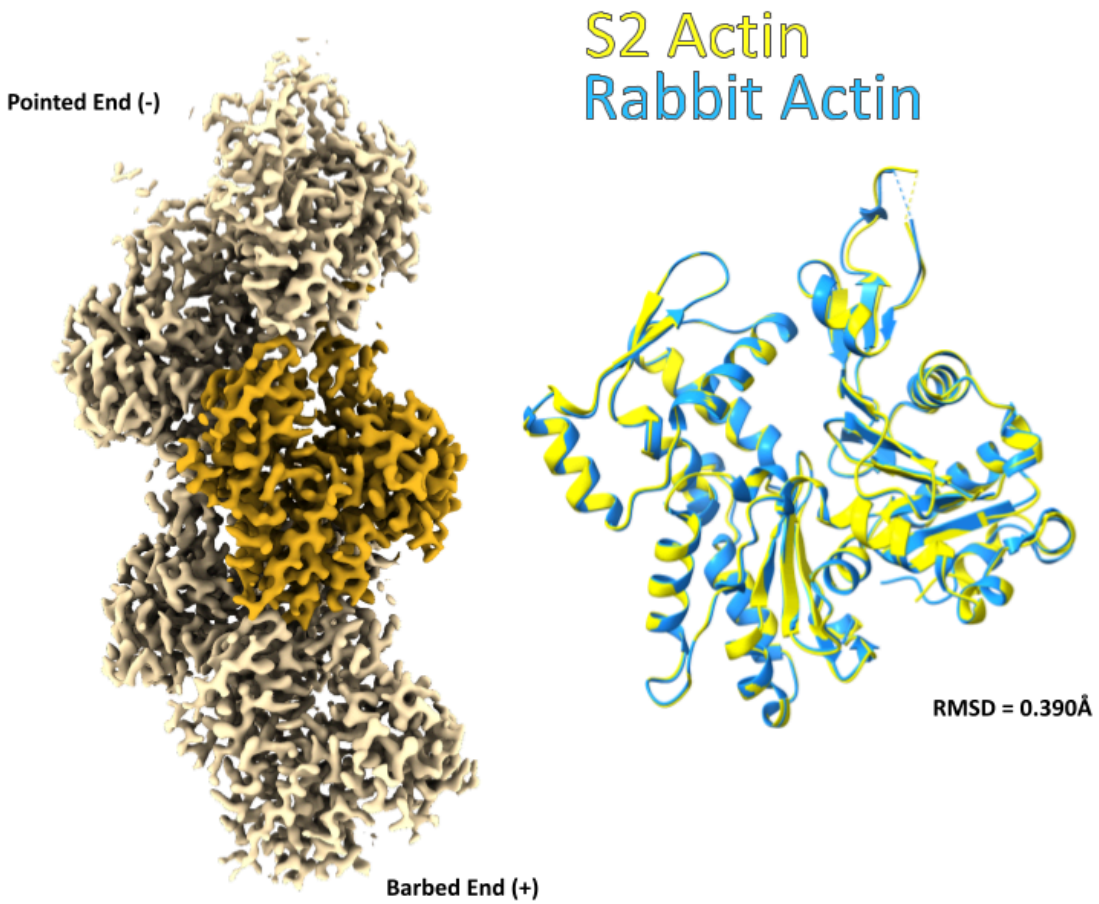

Figure 1.1 Drosophila filamentous actin reconstructed at high resolution
(Left) Electron density map of five monomers of the drosophila actin filament. Central monomer (which makes all possible inter-monomer interactions) colored darker yellow and polar ends labeled. (Right) Rabbit skeletal actin (PDBID: 8A2T) overlaid with experimental structure of S2 drosophila actin. Backbone RMSD calculated at 0.390 Å.

Isoform			
5C	SKRGILTLKYPIEHGIVTNWDDMEKIWHHT	90...	KIKII 331
42A	SKRGILTLKYPIEHGIVTNWDDMEKIWHHT	90...	KIKIV 331
79B	SKRGILSLKYPIEHGIITNWDDMEKVWHHT	90	
88F	SKRGILTLKYPIEHGIITNWDDMEKIWHHT	90	
57B	SKRGILTLKYPIEHGIITNWDDMEKIWHHT	90	
87E	SKRGILTLKYPIEHGIITNWDDMEKIWHHT	90	

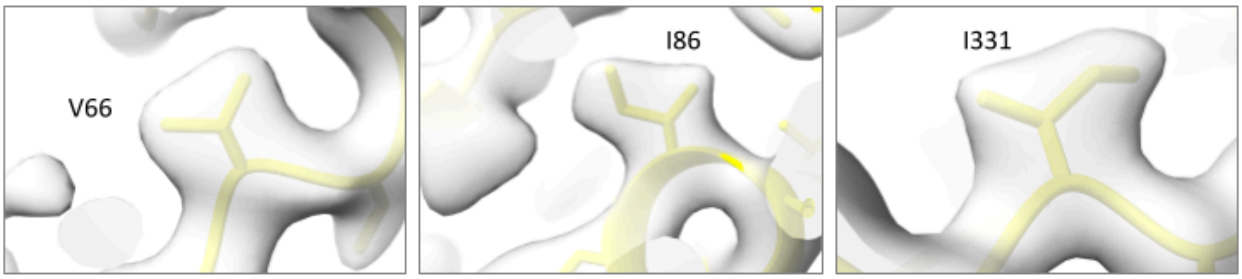

Figure 1.2 Drosophila actin isoform 5C identified through structure
(Top) Excerpt of divergent portions of aligned drosophila actin isoform sequences for its six isoforms, amino acids used for determining isoform highlighted. (Bottom) Highlighted amino acids are depicted with position in model and correlating portion of EM density map.

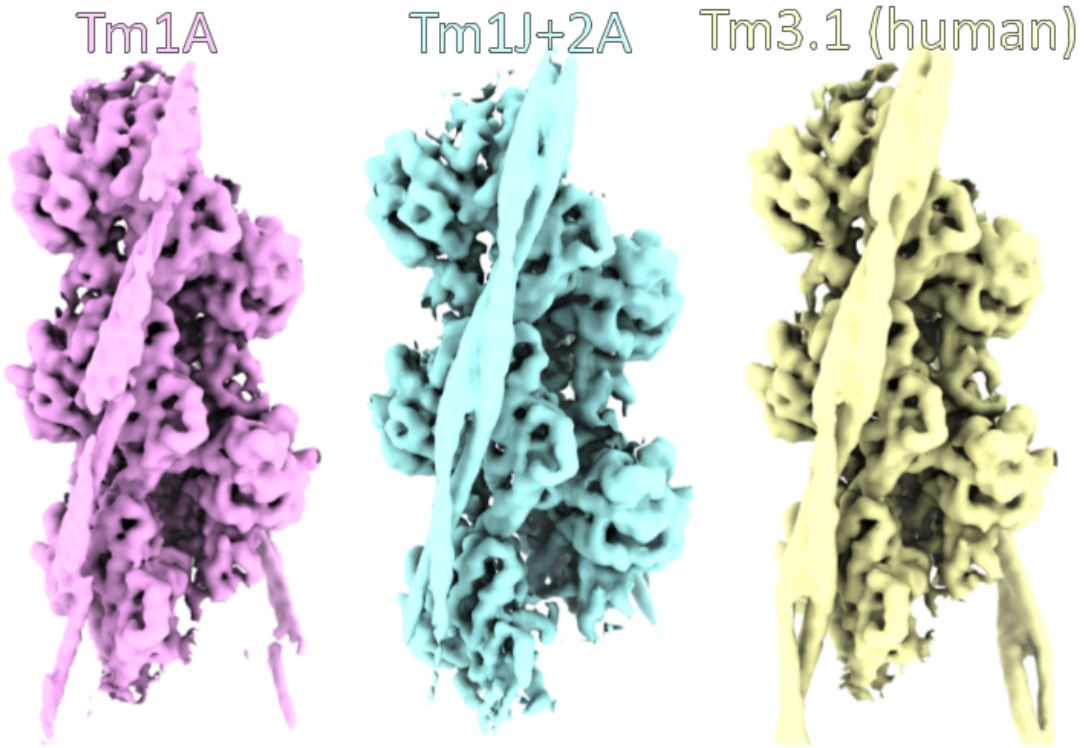

Figure 1.3 Helically refined structures of Drosophila tropomyosin coils 1A, 1J/2A, and human isoform 3.1
Unsharpened EM density maps of Drosophila tropomyosin 1A bound to S2 actin (pink, left), Drosophila tropomyosin heterodimer 1J/2A bound to S2 actin (blue, center), and human tropomyosin 3.1 bound to rabbit actin (yellow, right).

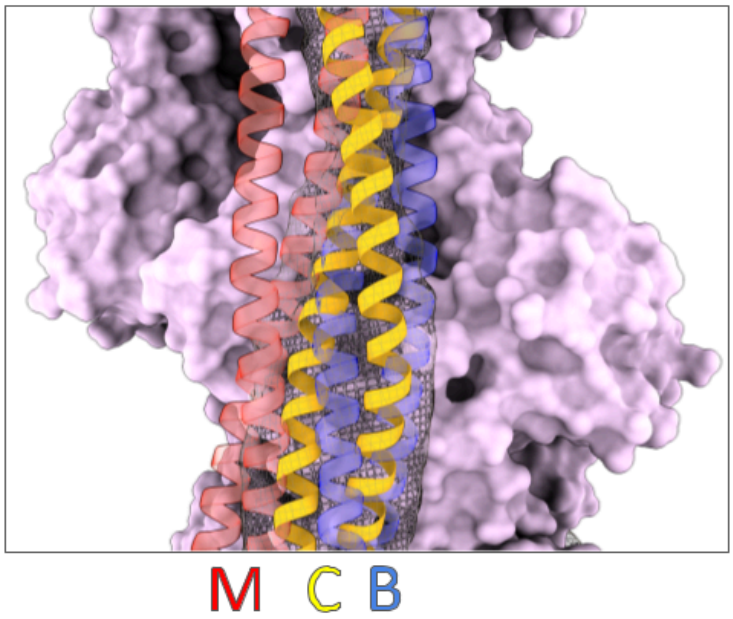

Figure 1.4 Drosophila tropomyosins 1A, and heterodimer 1J/2A both bind in the C-State in the absence of other actin-binding proteins
Depiction of tropomyosin binding postures along the actin filament. The M-state ("Myosin-bound" state) is represented by the red coiled-coil (PDBID: 5NOL). The C-state ("Closed" state) is represented by the yellow coiled-coil (model of Tm1A). The B-State is represented by the blue coiled-coil (PDBID: 5NOG). Tropomyosin coils 1A, 1J/2A, and 3.1 occupy the position of the yellow coil when the filament is composed of only actin and tropomyosin.

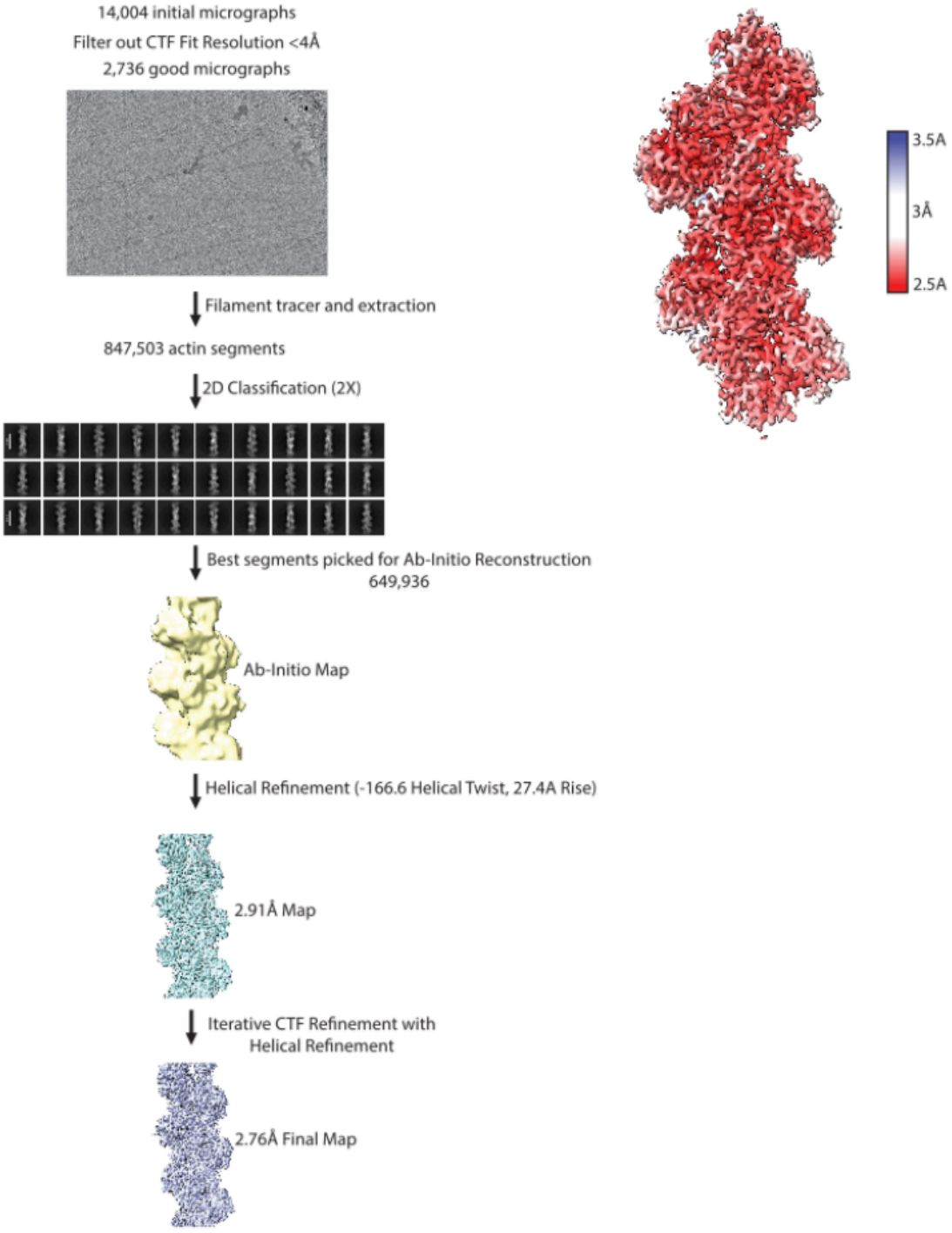

Figure 1.4 Cryo-EM workflow for resolving the structure of bare Drosophila actin 5C
(Left) Schematic workflow for the image processing done to reconstruct Drosophila actin. Particle counts (segments) are labeled and representative EM density maps are displayed for intermediate steps of the process. The final map possessed 2.76 Å global resolution with low local resolution in the D-Loop. (Right) Local resolution map of final reconstruction and color coded resolution scale.

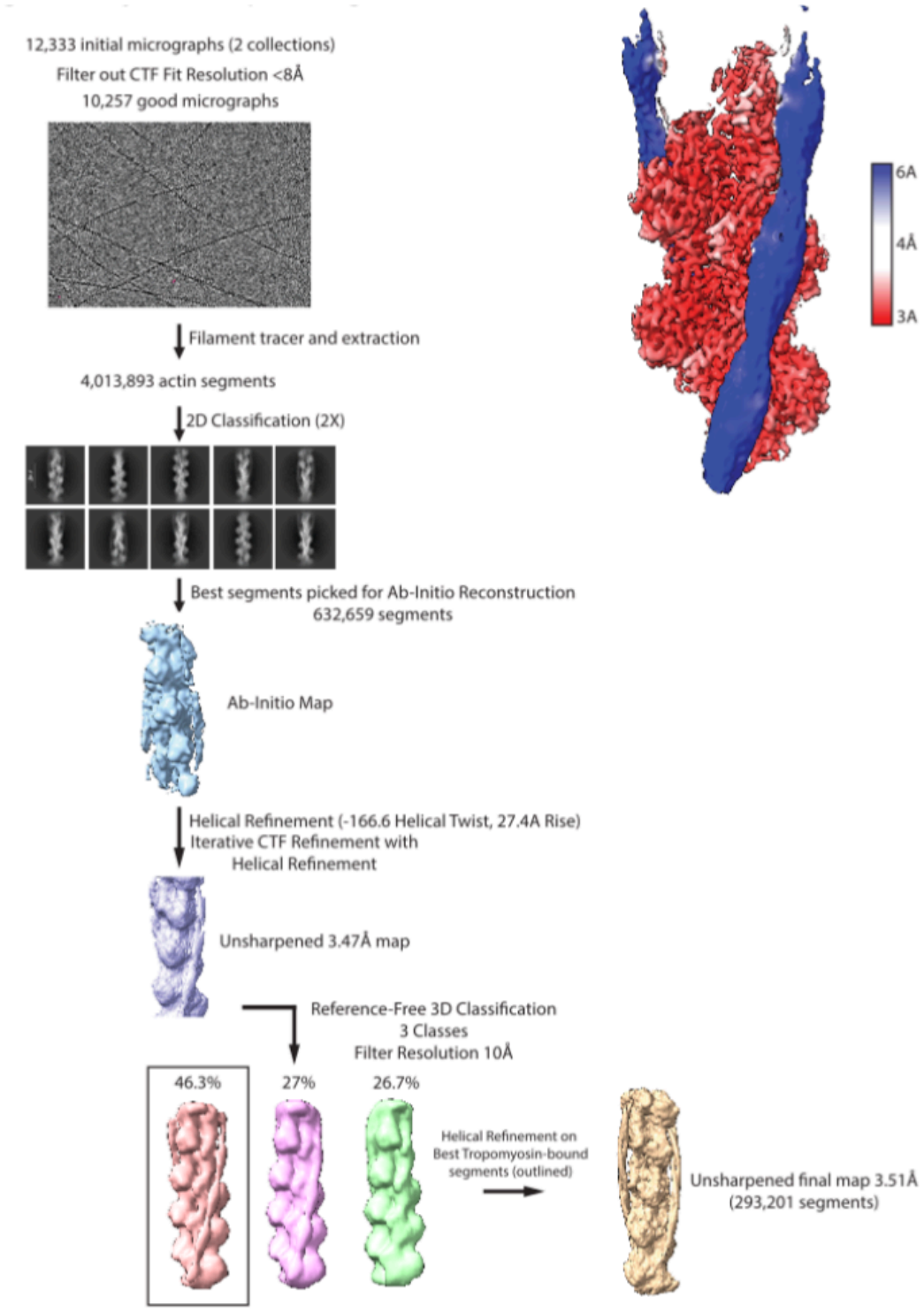

Figure 1.5 Cryo-EM workflow for resolving the structure of actins in complex with tropomyosin

(A) Depicted is an example schematic workflow for the image processing done to reconstruct tropomyosin bound to actin (using the workflow for Tm1A). Particle counts (segments) are labeled and representative EM density maps are displayed for intermediate steps of the process. **(B)** Local resolution map of final reconstruction and color coded resolution scale.

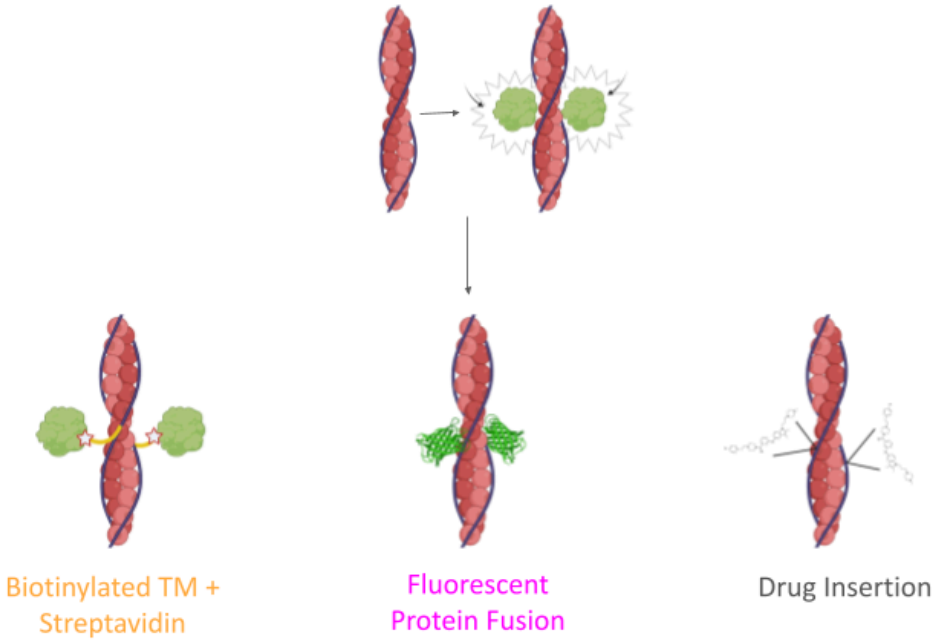

Figure 1.6 Proposed methods for adding a fiducial to tropomyosin
Cartoon representation of different methods of adding molecules which could break Tm symmetry and provide additional electron density. Tropomyosin-actin filaments would be solved using a single-particle workflow instead of applying helical symmetry.

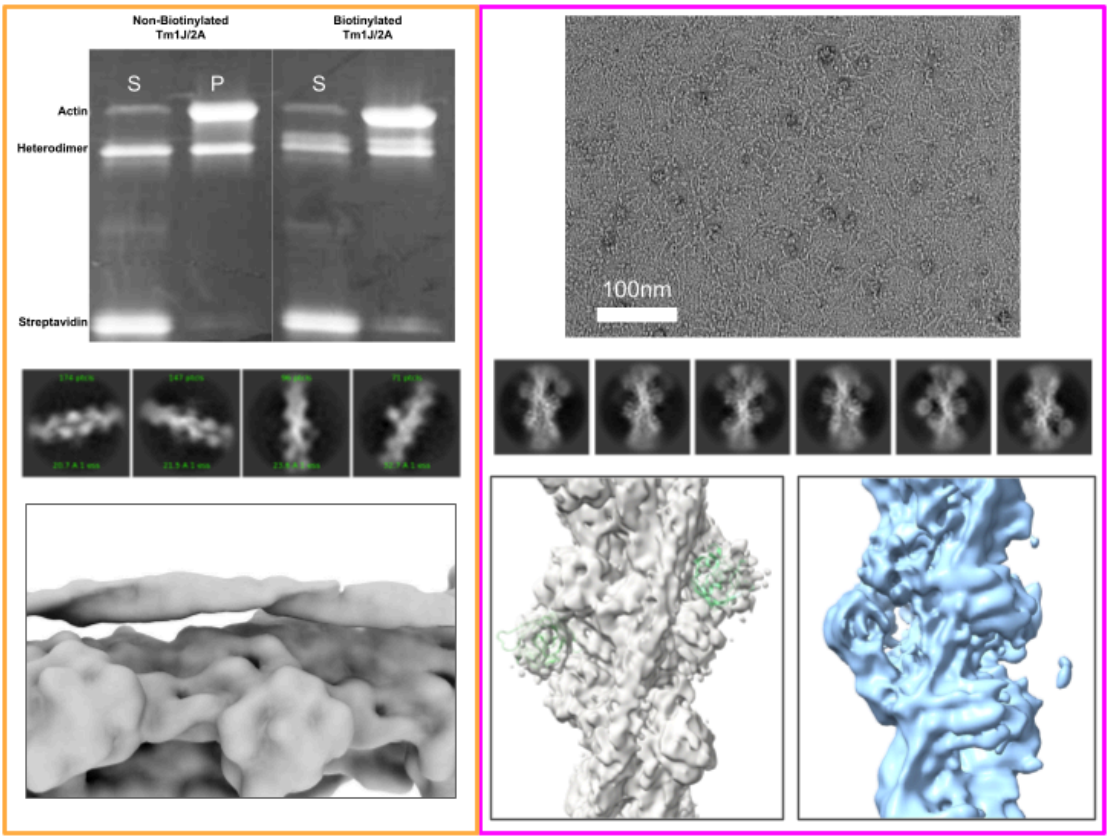

Figure 1.7 Fiducials successfully form actin-tropomyosin complex but do not help reconstruct tropomyosin to high resolution
Left, outlined in orange: Overview of the biotinylation+streptavidin method attempted; tropomyosin was successfully biotinylated and pulled down streptavidin in cosedimentation assay, but streptavidin density was blurry in 2D classes and unresolved in 3D reconstruction. Right, outlined in magenta: Overview of the GFP-tropomyosin fusion method attempted; GFP was readily N-terminally fused to tropomyosin and the full construct could be observed in Negative Stain EM. Although GFP-tropomyosin was able to generate 2D class averages with high resolution features in the flanking GFP densities, the final reconstruction of GFP-tropomyosin filaments showed no linkage or junction region proximal to the GFP.

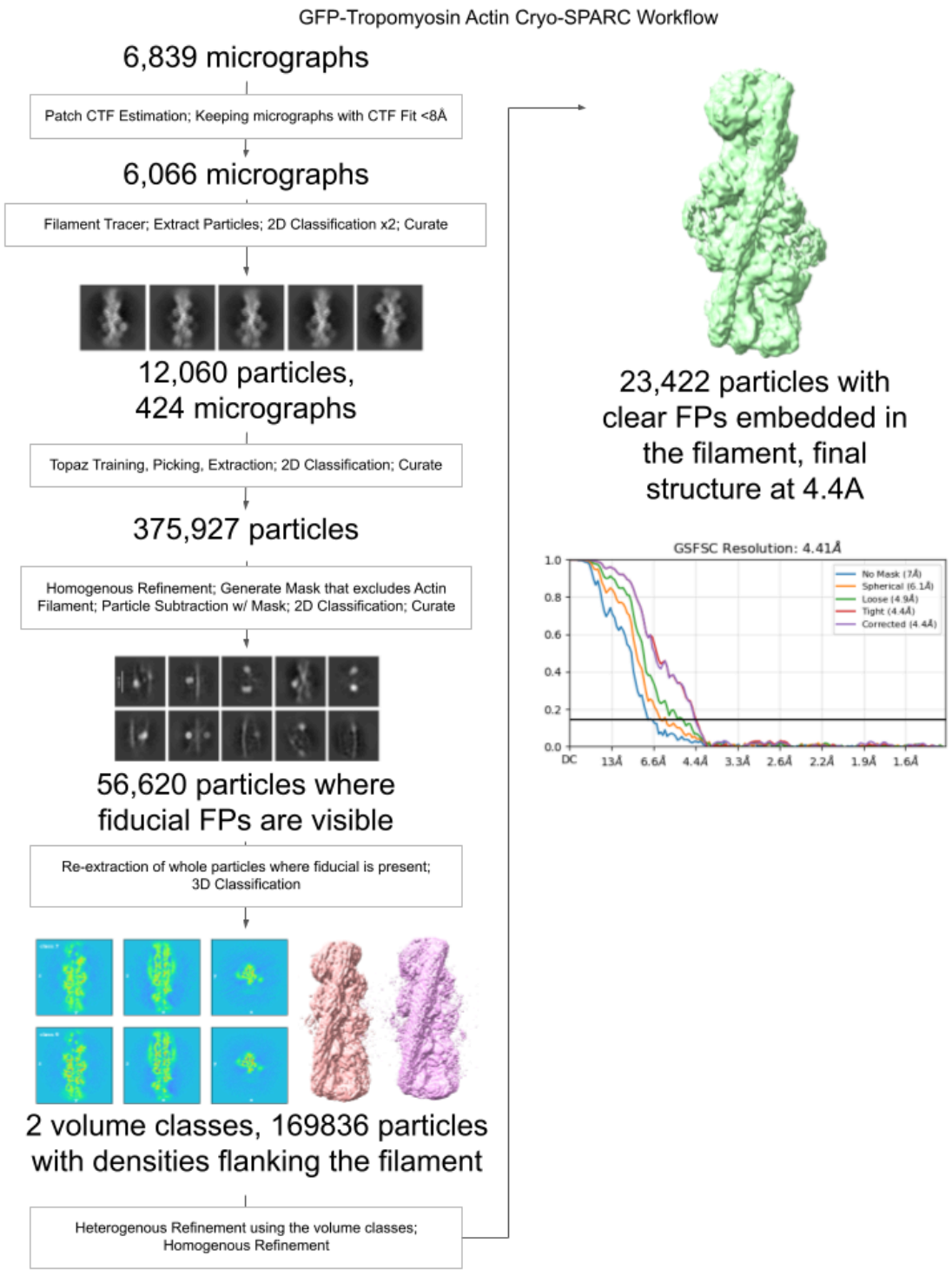

Figure 1.8 Data processing workflow to curate particles for reconstruction of GFP-tropomyosin

Schematic workflow for the image processing done to reconstruct actin-tropomyosin complex with GFP particles present. Particle counts (segments) are labeled and representative EM density maps are displayed for intermediate steps of the process.

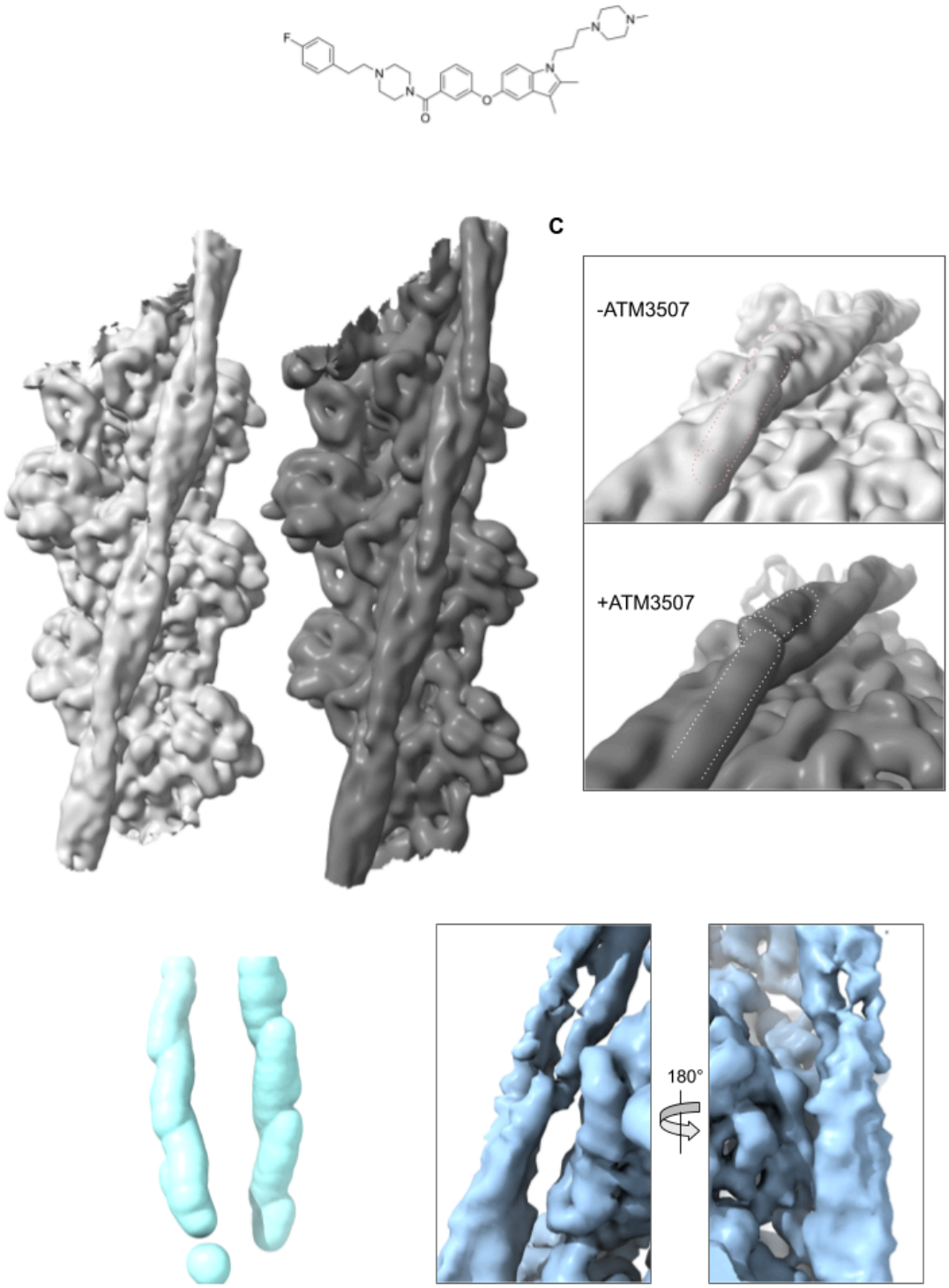

Figure 1.9 ATM3507 induces a symmetry break in the coiled-coil of Tm3.1 and enables rudimentary reconstruction of the junction region
(Top) Structural formula representation of ATM3507. (Middle Left) Unsharpened EM density maps of Tm3.1 bound to rabbit actin without (white) and with (gray) ATM3507 present. (figure caption continued on next page)

(figure caption continued from the previous page) (Middle Right) Closeup view of coiled-coil in the presence and absence of ATM3507. Cartoon overlay of alpha-helical tube added for clarity. (Bottom Left) Mask (light blue) used which encapsulated both coiled-coils. (Bottom Right) Structure of putative junction region after masking and heterogenous refinement.

Methods

Expression and Purification of Tropomyosin

Drosophila tropomyosins 1A, 1J, 2A were in the pet21b vector in E. coli BL21 star cells. Human tropomyosin 3.1 in the pet3b vector was generously gifted to us by Peter Gunning. All tropomyosin constructs possess an Alanine and Serine at the N-terminus to mimic the acetylation PTM and a 6his-SUMO tag (6his-SUMO-AS). eGFP and Cerulean3 were cloned into the construct N-terminal to AS mimic using a gene block.

All homodimeric tropomyosins (including fluorescent protein fusions) were purified with the following procedure:

Plasmid was transformed into E. coli BL21 star cells, grown in Terrific Broth, and induced for overexpression at OD_{600}=0.6-0.8 using 0.5-1mM IPTG. After induction, cells were then grown at 37C for 4 hours while shaking, then pelleted and flash frozen for storage at -80C.

Pellets of overexpressed cells were thawed and resuspended in Lysis Buffer (50mM Tris, 500mM KCl, 1mg/L of DNAse, 1mg/L of RNAse, 1mM PMSF, 1mM BME, 0.5mM EDTA, 10mM Imidazole, pH=8 at 4C). Lysis of cells was performed with two passes through a Microfluidizer at 12k psi, lysate was cleared with a 38k rpm spin for 1hr at 4C on a Beckman Type 45-Ti rotor. Cleared lysate was then injected onto Histrap Excel columns (3x5ml = 15ml total column volume) using an AKTA. The resin was washed with 10CV of Wash Buffer (10mM Tris, 500mM KCl, 10mM Imidazole, 0.5mM EDTA, 1mM BME, ph=8 at 4C), and eluted with a linear gradient totalling 20CV with gradually increasing concentration of Elution Buffer up to 100% (10mM Tris, 500mM KCl, 400uM Imidazole, 0.5mM EDTA, 1mM BME, ph=8 at 4C). After SDS-Page analysis the best fractions were pooled, and allowed to incubate with added

SUMO protease overnight at 4C, dialyzed against HA binding/wash buffer (5 mM Potassium Phosphate, 500 mM KCl, 0.5 mM TCEP, pH 7.5 at 4C).

Cleaved protein was run onto a BioRad hydroxyapatite CHT Type I 5ml cartridge using the AKTA. After a 10CV wash with HA binding buffer, a linear gradient to higher phosphate Elution buffer (200mM Potassium Phosphate, 500 mM KCl, 0.5 mM TCEP, pH 7.5 at 4C) was performed over 20CVs until Elution buffer reached 100% concentration. The cleanest Tm pool was collected, concentrated, and run through an Superdex 200 16/600 Gel Filtration column with Gel Filtration buffer (10mM Tris, 500mM KCl, 0.5mM TCEP, pH 7.5 at 4C). After gel filtration, tropomyosin fractions were concentrated and flash frozen for storage at -80C.

For biotinylation of tropomyosin, Thermo Scientific's EZ-Link Maleimide-PEG2-Biotin was used and manufacturer protocols were followed: A tenfold molar excess of Biotin reagent (suspended in PBS) was added to desalted tropomyosin solution and allowed to react overnight at 4C. Following desalting to remove extra reagent, labeling efficiency was validated using co-sedimentation assay (generally >98% efficiency).

Purification of Rabbit Actin

Rabbit actin was natively purified from rabbit muscle acetone powder. 10g of Pelfreeze Bio muscle acetone powder was suspended in 200ml of Buffer A (2mM Tris, 0.2mM ATP, 0.5mM TCEP, 0.04pct Azide, 0.1mM CaCl2). Suspended muscle acetone powder was stirred briskly without bubble formation at 4C for 30min with occasional mashing of the muscle material using a glass rod. The solution was then filtered through sterilized cheesecloth and spun down at 10k rpm at 4C for 1hr in a GSA rotor. The supernatant was once more filtered through sterile cheesecloth and volume was measured. 10X KMEI (100mM Imidazole pH 7, 500mM KCl, 10mM MgCl2, 10mM EGTA) was added until 1X concentration of KMEI was achieved to

induce polymerization of actin, ATP was also added to achieve 100uM concentration. Actin was allowed to polymerize at room temperature with gentle stirring for 30 minutes before adding solid KCl to 800mM and allowing the solution to sit at room temperature for another 30 minutes. The polymerized actin was then pelletted using a spindown in a Beckman Type 45-Ti rotor at 38k rpm for 1 hr at 4C. The resulting actin pellet would be clear and glassy. Using gentle encouragement with a glass rod and 5ml of Buffer A the pellet is resuspended and made to dialyze over the course of 3 days in Buffer A with daily buffer changes to let the actin depolymerize. Depolymerized material was spun down in Beckman TLA110 rotor to remove aggregates and polymerized material, and the cleared supernatant was gel filtered in an Superdex 200 16/600 Gel Filtration Column. The fractions corresponding to actin were collected and dialyzed against 20% sucrose Buffer A (cryoprotectant), then snap frozen and stored at -80C.

Expression and Purification of Gelsolin 4-6

The purification protocol to extract actin from S2 cells requires his-tagged gelsolin fragments containing the actin-binding region (4-6). Gelsolin fragment 4-6 was expressed on the pCold vector. Plasmid was transformed into E. coli BL21 star cells and grown in Terrific Broth before induction at OD_{600}=0.6-0.8 using 0.5mM IPTG. Induced cells were cooled down in icebaths and then allowed to grow overnight (<16hrs) shaking at 18C before harvesting/pelleting. Cell pellet was resuspended in Lysis Buffer (10mM Tris, 50mM KCl, 5mM CaCl2, 1mM ATP, 1mM BME, 1mM PMSF, ph8 at 4C), and then Pellets of overexpressed cells were thawed and resuspended in Lysis Buffer (50mM Tris, 500mM KCl, 1mg/L of DNAse, 1mg/L of RNAse, 1mM PMSF, 1mM BME, 0.5mM EDTA, 10mM Imidazole, pH=8 at 4C). Lysis of cells was performed with two passes through a Microfluidizer at 12k psi, lysate was cleared with a 38k rpm spin for 1hr at 4C on a Beckman Type 45-Ti rotor. Cleared lysate was then injected onto

Histrap Excel columns (3x5ml = 15ml total column volume) using an AKTA. The resin was washed with 10CV of Wash Buffer (10mM Tris, 50mM KCl, 25mM Imidazole, 5mM CaCl2, 1mM ATP, 1mM BME, ph=8 at 4C), and eluted with a linear gradient totalling 20CV with gradually increasing concentration of Elution Buffer up to 100% ((10mM Tris, 50mM KCl, 5mM CaCl2, 1mM BME, 200mM Imidazole, pH 8 at 4C).). After SDS-Page analysis the best fractions were pooled, concentrated, and run through a Superdex 200 16/600 Gel Filtration column with Buffer A. After gel filtration, gelsolin fractions were concentrated and stored overnight at 4C in dialysis against Buffer A until needed for the purification of S2 Actin.

Purification of Drosophila S2 Actin

Actin from Drosophila S2 cells were natively purified using the method previously pioneered by Johnny Rodriguez [x]. Approximately 8 liters of S2 cells were grown in SFM-II complete media and harvested yielding 70-90g worth of cell pellet.

Cell pellet was resuspended in Extraction Buffer (50mM Tris, 5mM CaCl2, 1mM ATP, 1mM DTT, 5mg/L Aprotonin, 40ug/ml Soybean Trypsin Inhibitor, 15mg/L Benzamidine, 10mg/L Leupeptin, 5mg/L Pepstatin, 1mM PMSF, ph8 at 4C) at a 2 to 1 buffer volume to pellet weight ratio. Using a tight dounce, the cell material was homogenized and lysed. S2 cell lysate was mixed with all purified Gelsolin 4-6 and solid KCl was added to achieve 50mM. This mixture was allowed to incubate together at 4C overnight with gentle stirring (binding step). After overnight binding, the gelsolin-S2 lysate mixture was spun down at 32krpm at 4C for 30min in a Beckman Type 45-Ti rotor (low speed spin), the supernatant of this spin was once again spundown at 45k rpm at 4C for 2hrs with the same Type 45-Ti rotor. The supernatant of this spindown was cleared of floating detritus and fat using a sterile and clean cheesecloth, and then was injected onto a 3x5ml (CV = 15ml) Histrap Excel column using an AKTA, at this

stage much of the gelsolin fragment has bound the actin from cell lysate.. The resin was washed with 10CV of Wash Buffer (10mM Tris, 50mM KCl, 5mM CaCl2, 1mM ATP, 1mM BME, ph=8 at 4C), and then washed with 10CV of a second Wash Buffer (10mM Tris, 50mM KCl, 5mM CaCl2, 1mM ATP, 1mM BME, 30mM Imidazole, ph=8 at 4C). The S2 actin was eluted through the removal of Calcium and subsequent release of actin from gelsolin; this was performed with a 20CV linear gradient towards 100% Actin Elution Buffer from Wash2 Buffer (Actin Elution Buffer: 10mM Tris, 50mM KCl, 1mM ATP, 1mM BME, 0.5mM EGTA, ph8 at 4C). The gelsolin was eluted using high imidazole through another 20CV linear gradient towards Gelsolin Elution Buffer from Actin Elution Buffer (Gelsolin Elution Buffer: 10mM Tris, 50mM KCl, 1mM ATP, 1mM BME, 300mM Imidazole, ph8 at 4C), After SDS-Page analysis the best actin-containing fractions were pooled and MgCl2 was added to 2mM to induce polymerization. The pooled actin was allowed to polymerize overnight at 4C. The actin was then spun down at 38krpm in a Beckman Type 45-Ti rotor for 1hr at 4C and the pellet which contains actin was dialyzed against Buffer A for three days to depolymerize (same as described in the rabbit actin prep protocol). This actin pellet was stubborn to depolymerize, so an additional sonication step was used to fully resuspend the pellet. Depolymerized material was spun down in Beckman TLA110 rotor to remove aggregates and polymerized material, and the cleared supernatant was gel filtered in an Superdex 200 16/600 Gel Filtration Column. The fractions corresponding to actin were collected and dialyzed against 20% sucrose Buffer A (cryoprotectant), then snap frozen and stored at -80C.

Cosedimentation Assay

Actin and tropomyosin were mixed in polymerizing conditions (100mM KCl, 1mM MgCl2, 1mM EGTA, 10mM HEPES, pH=7 at RT) at equimolar concentrations (5uM).

Depending on any additional binder proteins being assayed, the order of addition of protein would be modified to maximize formation of fully-formed actin-tropomyosin-binder complex (for example, allowing tropomyosin and actin to polymerize for >15min at RT before addition of antibody in order to prevent sequestration of tropomyosin from actin binding). Fully mixed reaction solution would be allowed to polymerize for 30minutes before spindown in a TLA100 rotor at 80krpm and 4C for 20min. Supernatant and pellet resuspended with equivalent volume of reaction were analyzed using SDS-Page to determine the quantity of pulled down protein.

Negative Stain EM

Polymerized samples were prepared by applying 2.5 L of protein sample to 200mesh Formvar carbon coated glow discharged grids and incubating for 30 seconds. Grids were washed with ddH20, blotting after washes. Grids were stained with 0.75% uranyl formate, blotting between applications. For the last staining step, the grid was incubated in stain for 30 seconds before blotting. Micrographs were taken with a Technai T12 microscopy with 120 kV voltage and a magnification of 48000. Images were taken with a Gatan 4k x 4k charge-coupled device camera.

Cryo-EM Screening and Data Collection

Rabbit actin and tropomyosin was co-polymerized at room temperature for 30 minutes with the following conditions: 3uM actin, 3uM Tpm3.1, 100mM KCl, 1mM MgCl2, 1mM EGTA, 10mM HEPES, ph = 7. For the structure saturated with ATM3507, 3uM of the drug was added at the beginning of the reaction. 300 Mesh Lacey Carbon on AU grids were glow discharged with a plasma cleaner. Vitrification was done using a Vitrobot, 3ul of sample was applied to grids and made to incubate for 15 seconds at room temperature before a 1 second blot using Whatman number 1 filter paper, followed by plunge freezing in liquid ethane. Grids were

screened and data was collected using an on-site Talos Arctica at 200keV equipped with a K3 detector (Gatan). Using SerialEM, micrographs were captured at a magnification of 45,000x in counting mode resulting in a pixel size of 0.865Å. Each exposure was 75 frames and a dose rate of 16e-/pix/s resulting in a nominal dose of 64.1e-/Å2. Data was collected at a defocus range of -1.0 to -2.0 um. 1,566 micrographs were collected this way for actin and tropomyosin alone, and 6,020 micrographs were collected with ATM3507 present.

Drosophila actin was polymerized at room temperature for 30 minutes with the following conditions: 10uM actin, 100mM KCl, 1mM MgCl2, 1mM EGTA, 10mM HEPES, ph = 7. R1.2/1.3 300 Mesh Quantifoil Carbon AU grids were glow discharged with a plasma cleaner. Vitrification was done using a Vitrobot, 3ul of sample was applied to grids and made to incubate for 15 seconds at room temperature before a 1 second blot using Whatman number 1 filter paper, followed by plunge freezing in liquid ethane. Grids were screened using an on-site Talos Arctica at 200keV before being sent to Janelia campus (Ashburn, Virginia) for data collection on a Titan Krios at 300keV with a 20keV Gatan energy filter and a K3 direct detector. Using SerialEM, images were taken at 105,000x magnification using super resolution, resulting in a pixel size of 0.4135Å, with a defocus range of -0.8 to -1.5um. At 60 frames per movie the total dose was 60e-/A2. 14,004 micrographs were collected this way for bare Drosophila actin.

CryoEM Data Processing

All acquired movies were motion-corrected using MotionCorr2. Motion-corrected datasets were imported and processed in cryoSPARC v4.0.2. Contrast transfer function (CTF) estimation was performed using cryoSPARC Patch CTF Estimation.

For bare Drosophila actin, we kept micrographs below 8Å maximum CTF fit resolution for further processing, resulting in a total of 1,109 micrographs for the next steps. CryoSPARC's

filament tracer job was used to pick segments of actin filaments from micrographs. After fourier cropped extraction, 352,576 segments were put into iterative 2D classification, the best particles from this were chosen to be re-extracted without cropping and used for ab-initio reconstruction (206,400 segments). Subsequent helical reconstruction was performed using the helical parameters of -166.6 Helical Twist (degrees) and Helical Rise of 27.4A. 3D Classification was used to remove segments lacking fully occupied tropomyosin, resulting in a final particle count of 68,670 for a final reconstruction at a global resolution of 4.35A.

Similarly for the ATM3507-bound actin: keeping all micrographs below 8Å maximum CTF fit resolution yielded a total of 5,385 micrographs for further processing. CryoSPARC's filament tracer job was used to pick particles representing segments of the actin filament, some overlap of segments was permitted as helical symmetry would be applied during reconstruction. After extraction and iterative 2D Classification, 454,706 segments were used for ab initio and then helical reconstruction of the actin filaments using the parameters of: Helical Twist of -166.6 (degrees), Helical Rise of 27.4Å. 3D Classification showed that the actin filaments were nearly completely saturated for tropomyosin binding. This yielded a structure of the actin-tropomyosin complex with ATM3507 present at 4.0Å global resolution.

Additional specific information for the data collected/processed can be found in Table 1.

Cryo-EM Model Building and Refinement

The model for our S2 actin density map was built by starting with an Alphafold predicted model of Drosophila actin isoform 5C monomer (AF-P10987-F1), the ADP and Mg2+ molecules were added using Coot within the ATPase binding pocket. Volume was manually erased from the filament map using UCSF ChimeraX until volume corresponding to a single monomer remained. This was used to rigid-body fit our initial model. Portions of the structure which had missing

density, such as part of the D-Loop and the N-terminus, were deleted manually.We then performed iterative refinement using Phenix real-space refine with secondary restraints as well as reference model restraints using PDBID: 8A2T as reference, followed by manual adjustments in Coot. After initial cycles we then removed geometry and reference restraints and improved map-to-model accuracy through further iterative refinement with Phenix and Coot. Once we obtained a satisfactory monomer structure, we modelled five monomers of actin into the filament map using rigid body fitting in order to capture all relevant inter-monomer contacts within the central subunit. A few rounds of refinement and manual adjustment yielded our final S2 actin structure. Given the low resolution of Tm1a (~6Å locally), we simply used an alanine backbone coiled-coil to represent the tropomyosin dimers (taken from PDBID: 5JLF). Tropomyosin structure was rigid-body fit into our S2 actin and Tm1A density map and minimal refinement was used to generate the final actin-tropomyosin structure. All depictions of cryo-EM density maps and protein structures were prepared using UCSF ChimeraX or UCSF Chimera.

References

Brooker, H. R., Geeves, M. A., & Mulvihill, D. P. (2016). Analysis of biophysical and functional consequences of tropomyosin-fluorescent protein fusions. FEBS letters, 590(18), 3111–3121.

Charles-Orszag, A., Petek-Seoane, N. A., & Mullins, R. D. (2024). Archaeal actins and the origin of a multi-functional cytoskeleton. Journal of bacteriology, 206(3), e0034823.

Chen, M., & Shen, X. (2007). Nuclear actin and actin-related proteins in chromatin dynamics. Current opinion in cell biology, 19(3), 326–330.

Currier, M. A., Stehn, J. R., Swain, A., Chen, D., Hook, J., Eiffe, E., Heaton, A., Brown, D., Nartker, B. A., Eaves, D. W., Kloss, N., Treutlein, H., Zeng, J., Alieva, I. B., Dugina, V. B., Hardeman, E. C., Gunning, P. W., & Cripe, T. P. (2017). Identification of Cancer-Targeted Tropomyosin Inhibitors and Their Synergy with Microtubule Drugs. Molecular cancer therapeutics, 16(8), 1555–1565.

Derman, A. I., Becker, E. C., Truong, B. D., Fujioka, A., Tucey, T. M., Erb, M. L., Patterson, P. C., & Pogliano, J. (2009). Phylogenetic analysis identifies many uncharacterized actin-like proteins (Alps) in bacteria: regulated polymerization, dynamic instability and treadmilling in Alp7A. Molecular microbiology, 73(4), 534–552.

Gateva, G., Kremneva, E., Reindl, T., Kotila, T., Kogan, K., Gressin, L., Gunning, P. W., Manstein, D. J., Michelot, A., & Lappalainen, P. (2017). Tropomyosin Isoforms Specify Functionally Distinct Actin Filament Populations In Vitro. Current biology : CB, 27(5), 705–713.

Goins, L. M., & Mullins, R. D. (2015). A novel tropomyosin isoform functions at the mitotic spindle and Golgi in Drosophila. Molecular biology of the cell, 26(13), 2491–2504.

Gunning, P., O'Neill, G., & Hardeman, E. (2008). Tropomyosin-based regulation of the actin cytoskeleton in time and space. Physiological reviews, 88(1), 1–35.

Huxley, H.E. (1973). Structural changes in the actin- and myosin-containing filaments during contraction. Cold Spring Harbor Symposia on Quantitative Biology, 37, 361–376.

Jansen, S., & Goode, B. L. (2019). Tropomyosin isoforms differentially tune actin filament length and disassembly. Molecular biology of the cell, 30(5), 671–679.

Hayakawa, K., Tatsumi, H., & Sokabe, M. (2012). Mechano-sensing by actin filaments and focal adhesion proteins. Communicative & integrative biology, 5(6), 572–577.

Ly, T., Krieger, I., Tolkatchev, D., Krone, C., Moural, T., Samatey, F. A., Kang, C., & Kostyukova, A. S. (2018). Structural destabilization of tropomyosin induced by the cardiomyopathy-linked mutation R21H. Protein science : a publication of the Protein Society, 27(2), 498–508.

Monteiro, P. B., Lataro, R. C., Ferro, J. A., & Reinach, F.deC. (1994). Functional alpha-tropomyosin produced in Escherichia coli. A dipeptide extension can substitute the amino-terminal acetyl group. The Journal of biological chemistry, 269(14), 10461–10466.

Muller, J., Oma, Y., Vallar, L., Friederich, E., Poch, O., Winsor, B. (2005). Sequence and comparative genomic analysis of actin-related proteins. Molecular Biology of the Cell, 16(12), 5736-5748.

Oosterheert, W., Klink, B. U., Belyy, A., Pospich, S., & Raunser, S. (2022). Structural basis of actin filament assembly and aging. Nature, 611(7935), 374–379.

Pollard T. D. (2008). Progress towards understanding the mechanism of cytokinesis in fission yeast. Biochemical Society transactions, 36(Pt 3), 425–430.

Pollard, T. D., & Borisy, G. G. (2003). Cellular motility driven by assembly and disassembly of actin filaments. Cell, 112(4), 453–465.

Rao, J. N., Rivera-Santiago, R., Li, X. E., Lehman, W., & Dominguez, R. (2012). Structural analysis of smooth muscle tropomyosin α and β isoforms. The Journal of biological chemistry, 287(5), 3165–3174.

Risi, C. M., Belknap, B., White, H. D., Dryden, K., Pinto, J. R., Chase, P. B., & Galkin, V. E. (2022). High-resolution cryo-EM structure of the junction region of the native cardiac thin filament in relaxed state. PNAS nexus, 2(1), pgac298.

Risi, C., Eisner, J., Belknap, B., Heeley, D. H., White, H. D., Schröder, G. F., & Galkin, V. E. (2017). Ca2+-induced movement of tropomyosin on native cardiac thin filaments revealed by cryoelectron microscopy. Proceedings of the National Academy of Sciences of the United States of America, 114(26), 6782–6787.

Röper, K., Mao, Y., & Brown, N. H. (2005). Contribution of sequence variation in Drosophila actins to their incorporation into actin-based structures in vivo. Journal of cell science, 118(Pt 17), 3937–3948.

Tripet, B., Van Eyk, J. E., & Hodges, R. S. (1997). Mapping of a second actin-tropomyosin and a second troponin C binding site within the C terminus of troponin I, and their importance in the Ca2+-dependent regulation of muscle contraction. Journal of molecular biology, 271(5), 728–750.

Xu, C., Craig, R., Tobacman, L., Horowitz, R., & Lehman, W. (1999). Tropomyosin positions in regulated thin filaments revealed by cryoelectron microscopy. Biophysical journal, 77(2), 985–992.

Xu, T., Verhagen, M. P., Teeuwssen, M., Sun, W., Joosten, R., Sacchetti, A., Ewing-Graham, P. C., Jansen, M. P. H. M., Boere, I. A., Bryce, N. S., Zeng, J., Treutlein, H. R., Hook, J., Hardeman, E. C., Gunning, P. W., & Fodde, R. (2024). Tropomyosin1 isoforms underlie epithelial to mesenchymal plasticity, metastatic dissemination, and resistance to chemotherapy in high-grade serous ovarian cancer. Cell death and differentiation, 31(3), 360–377.

Yamada, Y., Namba, K., & Fujii, T. (2020). Cardiac muscle thin filament structures reveal calcium regulatory mechanism. Nature communications, 11(1), 153.

Zhu, R., Yin, L., Zhou, R., & Zhang, X. (2025). Tropomyosin-1 positively regulates TGF-β/Smad3 signaling through STUB1 in arecoline-induced oral submucosal fibrosis. Odontology, 10.1007/s10266-025-01244-9. Advance online publication.

Chapter 2: Structural Determination of DNA Binding Location on Arp2/3 Complex

Introduction

Actin is a well-conserved cytoskeletal building block which assembles into filaments that then become part of higher-order networks to accomplish a variety of critical cellular functions such as motility, division, and endocytosis (Hatano and Oosawa, 1966; Pollard et al., 2000, Pollard and Borisy, 2003; Hinze et al., 2018). Several actin-regulating proteins, such as Arp2/3 complex, cofilin, and tropomyosin, are necessary to direct actin filaments towards morphologies and function. Due to their clinical relevance and universal importance to cells, many of actin's functions have been well-studied and characterized. However, the same is not true of actin's mysterious role in the nucleus, which has only recently begun to be elucidated.

One of the earliest discoveries of nuclear actin function was in Xenopus oocytes where networks of actin provided structure to the nucleus (Bohnsack, 2006). Later work in human neuronal cells using specific actin labeling revealed actin filament formation at the sites of double-stranded DNA damage, with the knockdown of nuclear actin import reducing the efficacy of DNA damage repair (Belin et al., 2015). Emerging evidence from further investigations has shown that this actin localized to DNA damage depended upon the Arp2/3 complex, an actin nucleator which is traditionally associated with branched-actin networks in the cytoplasm (Caridi et al., 2018; Schrank et al., 2018). Recent work in our lab has established that the Arp2/3 complex is capable of direct binding of DNA in vitro (unpublished). Chemical crosslinking experiments suggested three monomers of the Arp2/3 complex (ArpC1, Arp2, and Arp3) were primarily responsible for this DNA binding activity. In this chapter, I present a cryo-EM reconstruction of the Arp2/3 complex bound to single-stranded DNA which validates our prior observations and provides clues for Arp2/3's function at sites of DNA damage repair.

Results

To investigate the binding location of DNA on the Arp2/3 complex, we first performed psoralen DNA-protein UV crosslinking on Arp2/3 complex followed by western blot (Figure 2.1). We searched for band shifts which represented protein-DNA crosslinking events. From this assay we predicted ArpC1, Arp2, and Arp3 to be interacting with DNA. We note that crosslinking with ArpC1 generated a discrete band, but Arp2 and Arp3 were only able to generate high molecular weight smears, suggesting a weaker interaction between DNA and subunits Arp2 and Arp3 as compared to ArpC1. To better understand the structural orientation of the bound DNA, we performed cryo-electron microscopy (cryo-EM) on apo state and ssDNA-bound Acanthamoeba Arp2/3 complex. We prepared samples of Arp2/3 complex in the ssDNA-bound condition by incubating Arp2/3 complex with a 60mer ssDNA-optimized oligonucleotides for 30 minutes at room temperature before vitrification. Using these samples we were able to resolve ~3.8Å global resolution reconstructions of both unbound and bound conditions (Figures 2.2-2.6)(Table 2). These structures revealed two major density differences between apo and ssDNA-bound Arp2/3 complexes which are located in the cleft between ArpC1 and Arp2 and along the long alpha helix of Arp3. We used unsharpened maps to visualize both reconstructions because post-processing resulted in the loss of density differences without significant gain in their interpretability. We hypothesized that these EM densities corresponded to bound ssDNA on the Arp2/3 complex. These potential ssDNA binding locations agreed with our anisotropy data (unpublished, not shown) showing competition with N-WASP because of N-WASP's proximal binding to the ssDNA densities (Figure 2.2). To improve the resolution of the complex at the ArpC1-Arp2 cleft, we also attempted local refinement of ArpC1 and Arp2 using a mask which excluded Arp3 and ArpC3. The locally refined maps improved the

resolution and interpretability of the cleft between ArpC1 and Arp2 but could not delineate the structure of the ssDNA, potentially due to inherent flexibility, inconsistent binding, or heterogeneity of nucleotides interacting at the binding site. We generated a subcomplex model of ArpC1, Arp2, and Arp3 using Alphfafold. Using the Alphafold model and our reconstructions we analyzed the residues which likely interacted with the ssDNA at these putative binding locations and found groupings of basic, positively charged side chains that are exposed to solvent (Figure 2.2). On ArpC1 these residues include K141, K144, and K147. On Arp2 the putative DNA-binding residues are K332, K337, K339, and R341. On Arp3 we identified K341, R342, R345, K348, and R357. Sequence alignments of ArpC1, Arp2, and Arp3 across multiple species including humans demonstrated that these basic residues are well-conserved. We additionally used Paradock to generate DNA docked positions on the Arp2/3 complex using 6YW6 as an input structure (Banitt and Wolfson, 2011); out of ten docked positions, six were located within this cleft which agrees with our findings (Figure 2.2). Taken together, we conclude that Arp2/3 binds to DNA via a positively charged cleft between ArpC1 and Arp2, and a positively charged patch along Arp3's long helix.

Discussion

DNA double-strand breaks constantly occur in our cells due to genotoxins and physiological processes. These breaks must be repaired in a timely manner, or they can result in genomic instability or cell death. A cell must detect the lesion and recruit the correct repair proteins to the site of DNA damage. The two main pathways for DNA double-strand break repair are NHEJ and HDR. NHEJ is more error prone and can occur in any phase of the cell cycle, whereas HDR has higher fidelity, but can only occur during S or G2 phase when there is a sister chromatid template. Previous studies have shown that the Arp2/3 complex is involved in HDR and have suggested there is no involvement in NHEJ. Our structure shows that Arp2/3's role at sites of DNA damage extends beyond simply acting as an actin nucleator.

In our data, DNA competes for the binding regions of N-WASP on the Arp2/3 complex, but prior data has demonstrated that it is unable to activate Arp2/3 on its own (unpublished). It is likely that the co-localization of Arp2/3 and DNA is directing actin network formation at sites of DNA damage repair. We evaluate several potential models, which are not necessarily mutually exclusive, to explain the biological function of Arp2/3 DNA binding activity.

Branched-network assembly could function in a similar fashion as in Xenopus oocytes: acting as a physical net to contain the components necessary for DNA damage repair. Not exclusive to this framework, the actin network generated by Arp2/3 may act as a scaffold for DNA damage repair proteins by facilitating recruitment and maintenance of these proteins at sites of double-stranded breaks. In mammalian cells, DNA double-strand breaks appear to move around and form clusters (Schrank et al., 2018). These clusters may be the formation of repair centers that could help facilitate efficient repair of DNA damage because of the high concentration of repair proteins or help with searching for homology during HDR.

A commonly proposed mechanism for Arp2/3-mediated DNA damage repair is force generation via actin polymerization appropriated to either push the strand broken region to the periphery of the nucleus or to bring together broken ends of DNA. It is unlikely that this is the principal function of Arp2/3 in DNA damage due to the directional randomness of force generated by this type of actin nucleation, making it dubious that such a force could localize DNA meaningfully.

It has been shown that polymerization of actin filaments can deform phase condensates of VASP, an actin polymerase, *in vitro* (Graham et al., 2023). Applied within the nuclear context, Arp2/3-mediated actin nucleation, targeted to sites of DNA damage, may serve to locally disperse nuclear condensates which contain DNA damage repair machinery. Sequestration of actin via polymerization from bound chromatin remodeler complexes could also create an actin "sink" to activate these complexes.

Given the random directional nature of Arp2/3 force generation, it is conceivable that its role within the nucleus is to induce increased random motion of the large chromatin substrates, functionally improving the rate at which broken DNA strands and repair components meet in the correct conformation to begin repair. A very recent study has shown that the Arp2/3 complex is critical for improving chromosome mobility to allow loose strands to search for homology (Zhou et al., 2025). At present we believe this mobility model for Arp2/3's role in the nucleus is the most supported.

The work we have done with the Arp2/3 complex has helped illuminate the mechanism by which actin assembly may occur during the repair of DNA double-strand breaks. We showed that single stranded DNA binds in regions competing with NPFs, suggesting that Arp2/3 is not nucleating while bound to a loose DNA strand. Future work can focus on understanding how

DNA binding activity is critical to Arp2/3's function in the context of general DNA double-strand break repair.

Table 2.1 Arp2/3 CryoEM data collection, processing, and validation

	Apo Arp2/3	Arp2/3 + ssDNA
Data collection and processing		
Magnification	45,000	45,000
Voltage (kV)	200	200
Electron Exposure (e-/A^2)	64.1	64.1
Defocus Range (μM)	-1.0-2.0	-1.0-2.0
Pixel Size (Å)	0.865	0.865
Initial Micrographs	7,101	5,034
Final Particle Count	525,475	446,362
Map Resolution (FSC threshold 0.143)	3.90	3.94
Refinement (Phenix)		
Initial Model Used	Composite of Alfafold and homology	
Model Resolution (FSC threshold 0.5)	4.3	
Map CC (Volume)	0.56	
B Factor ($Å^2$)	245	
Validation		
MolProbity Score	2.06	
All-Atom Clashscore	4.85	
Rotamer Outliers	0.39	
C-Beta Outliers	0.00	
Ramachandran Plot		
Favored (%)	95.09	
Allowed (%)	4.85	
Outliers (%)	0.06	

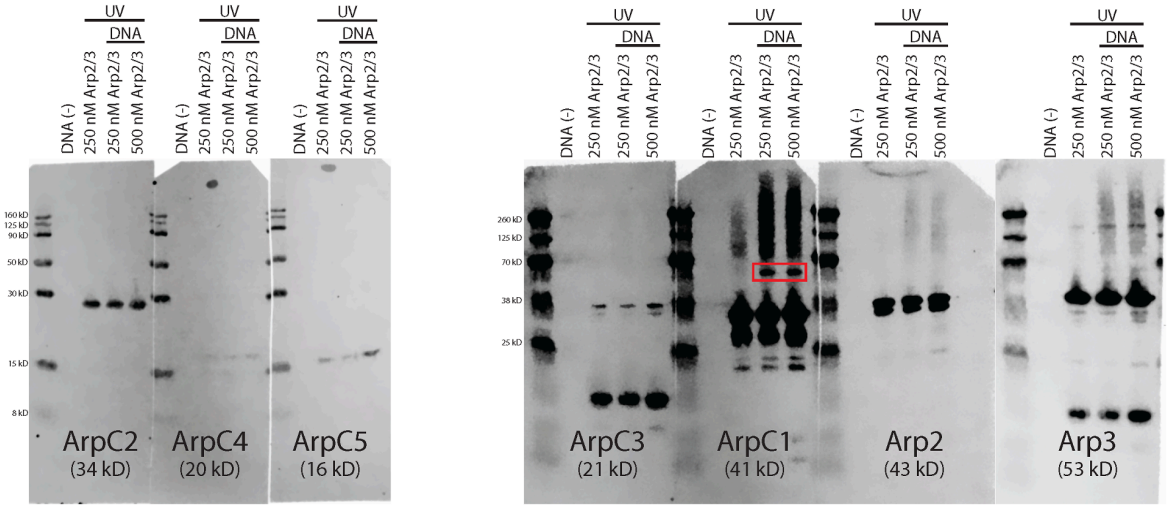

Figure 2.1 Arp2/3 complex crosslinks with DNA at subunits ArpC1, Arp2, and Arp3
Western blot of Porcine Arp2/3 subunits after DNA-protein UV crosslinking in the presence of NHS-psoralen. Appearance of higher molecular weight bands indicates covalent binding to psoralen-DNA. Notable bands were observed with the ArpC1 subunit as noted with the red box. Higher molecular weight smears also appeared when probing for the Arp2 and Arp3 subunits. Conditions: 40 BP DNA concentration: 100 nM; Arp2/3 concentration: 250 nM or 500 nM (as indicated); Buffer: 20 mM Tris pH 7.5, 25 mM KCl, 1 mM MgCl2, 1 mM DTT.

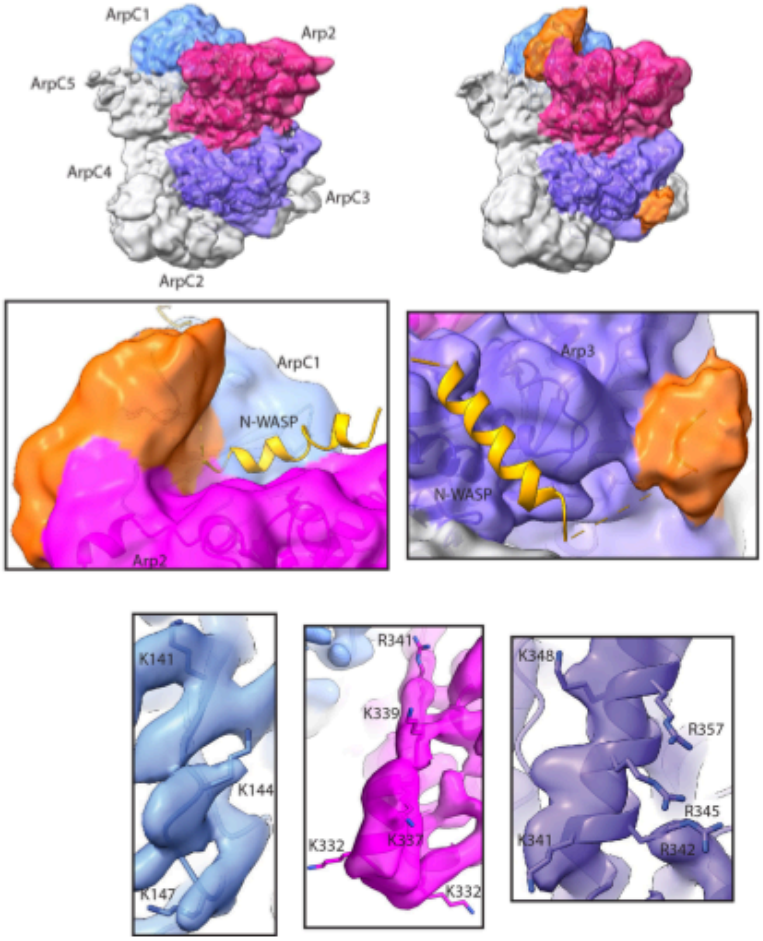

Figure 2.2 Structure of Arp2/3 complex shows DNA binds at patches of positive charge in direct competition with N-WASP VCA

Cryo-EM reconstructions of apo (top left) and ssDNA-bound Arp2/3 complex (top right). Models of Acanthamoeba ArpC1, Arp2, and Arp3 are rigid-body fitted. Subunits of the Arp2/3 complex are labeled. ArpC1, Arp2, and Arp3 are colored teal, magenta, and indigo, respectively. Orange densities represent ssDNA: located in the cleft between ArpC1 and Arp2 as well as along the long alpha helix of Arp3. (Middle) Close-up view of ss-DNA densities at the ArpC1/2 cleft (left) and along Arp3 (right) with binding position of N-WASP VCA (PDBID:6UHC) shown to be in competition. (Bottom) Close-up view of conserved positively charged residues at locations of DNA binding in ArpC1 (left), Arp2 (middle), and Arp3 (right).

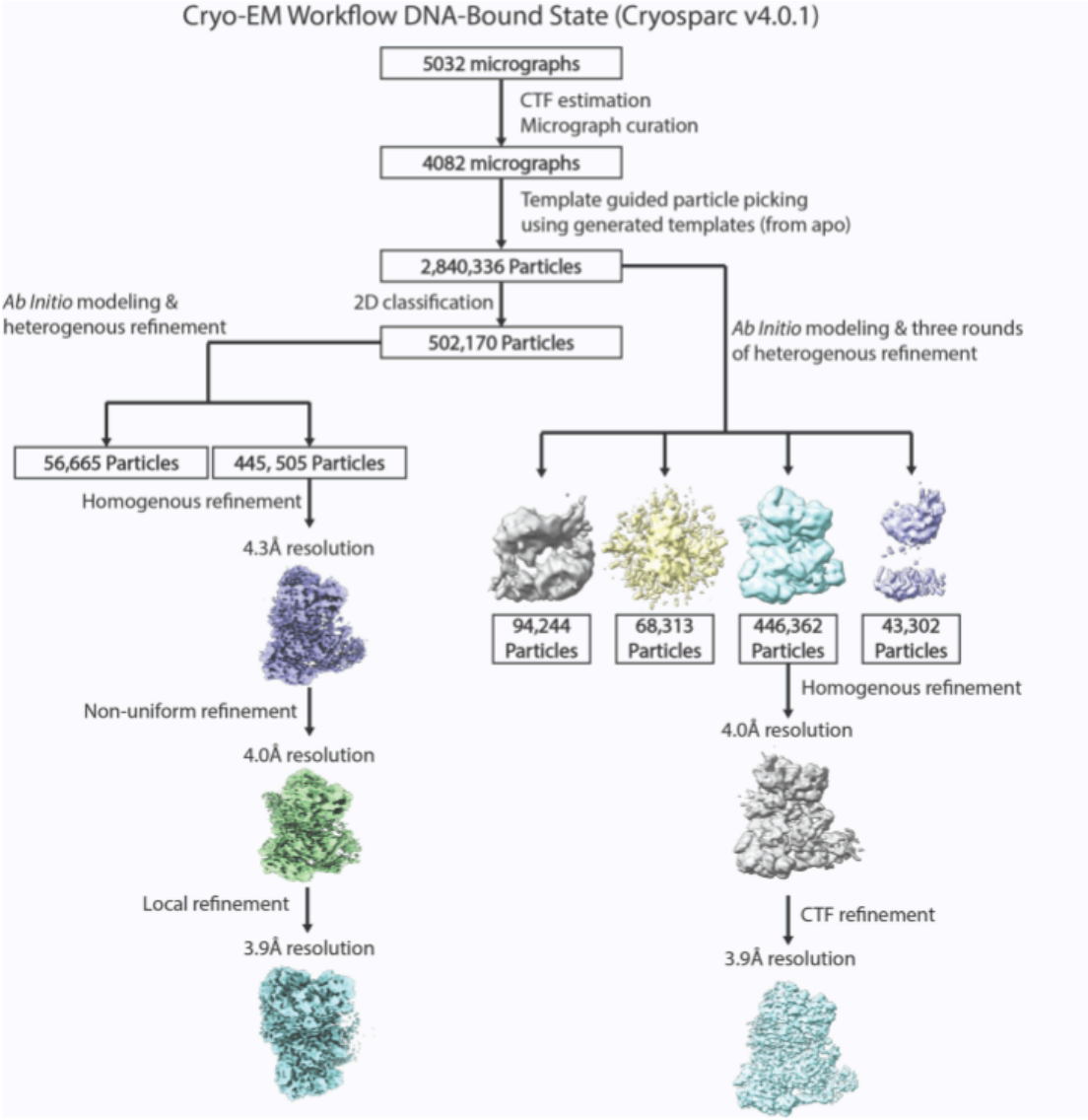

Figure 2.3 Cryo-EM workflow for resolving the structure of DNA-bound Arp2/3 complex
Schematic workflow for the image processing done to reconstruct Arp2/3 bound to DNA. Particle counts are labeled and representative EM density maps are displayed for intermediate steps of the process.

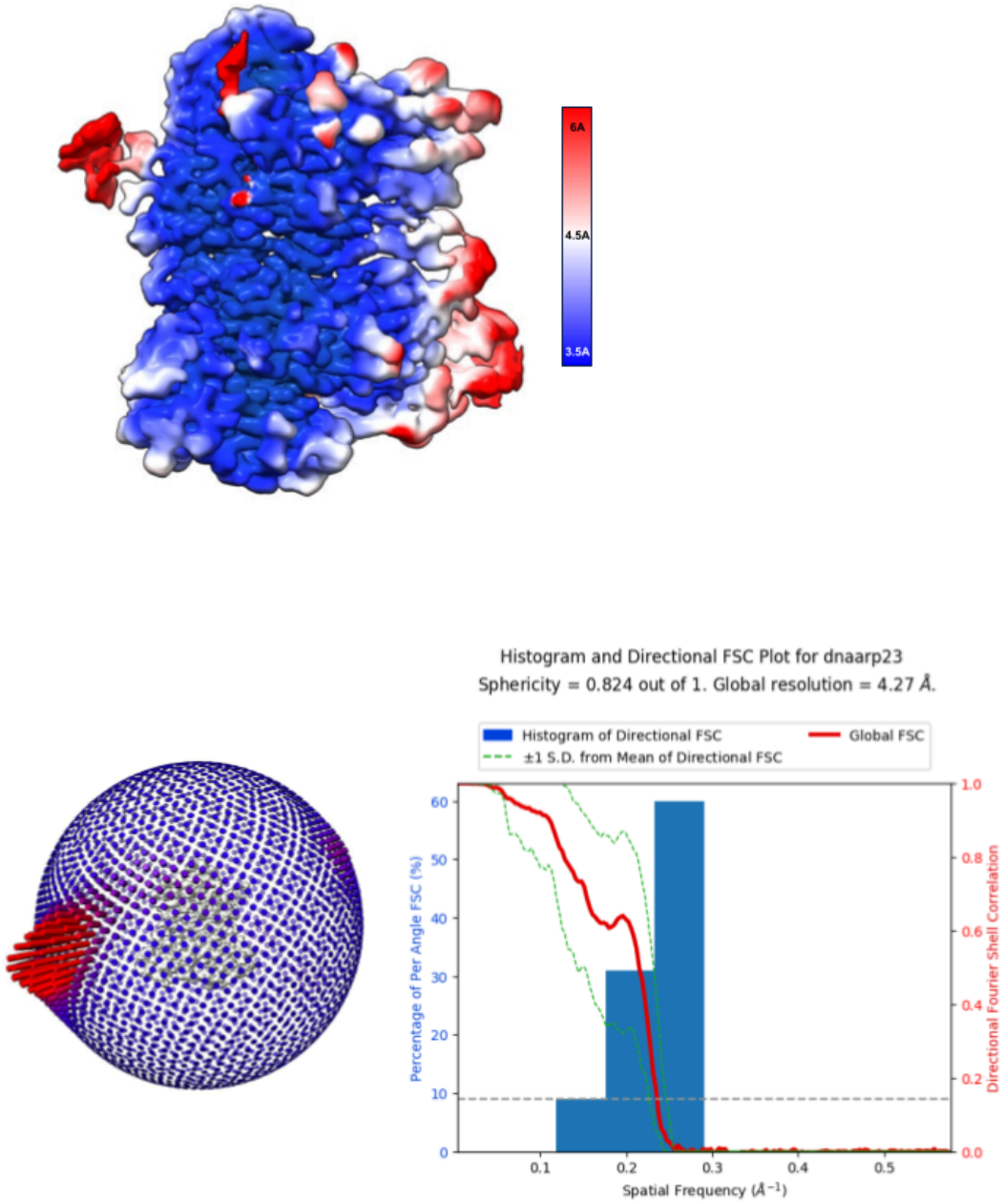

Figure 2.4 Local resolution map and map quality for Arp2/3 with DNA
(Top) Local resolution map of Arp2/3 complex with bound DNA. Color key provided. (Bottom Left) Angular distribution representation of structure. (Bottom Right) 3DFSC histogram of structure with a global resolution of 4.27 Å.

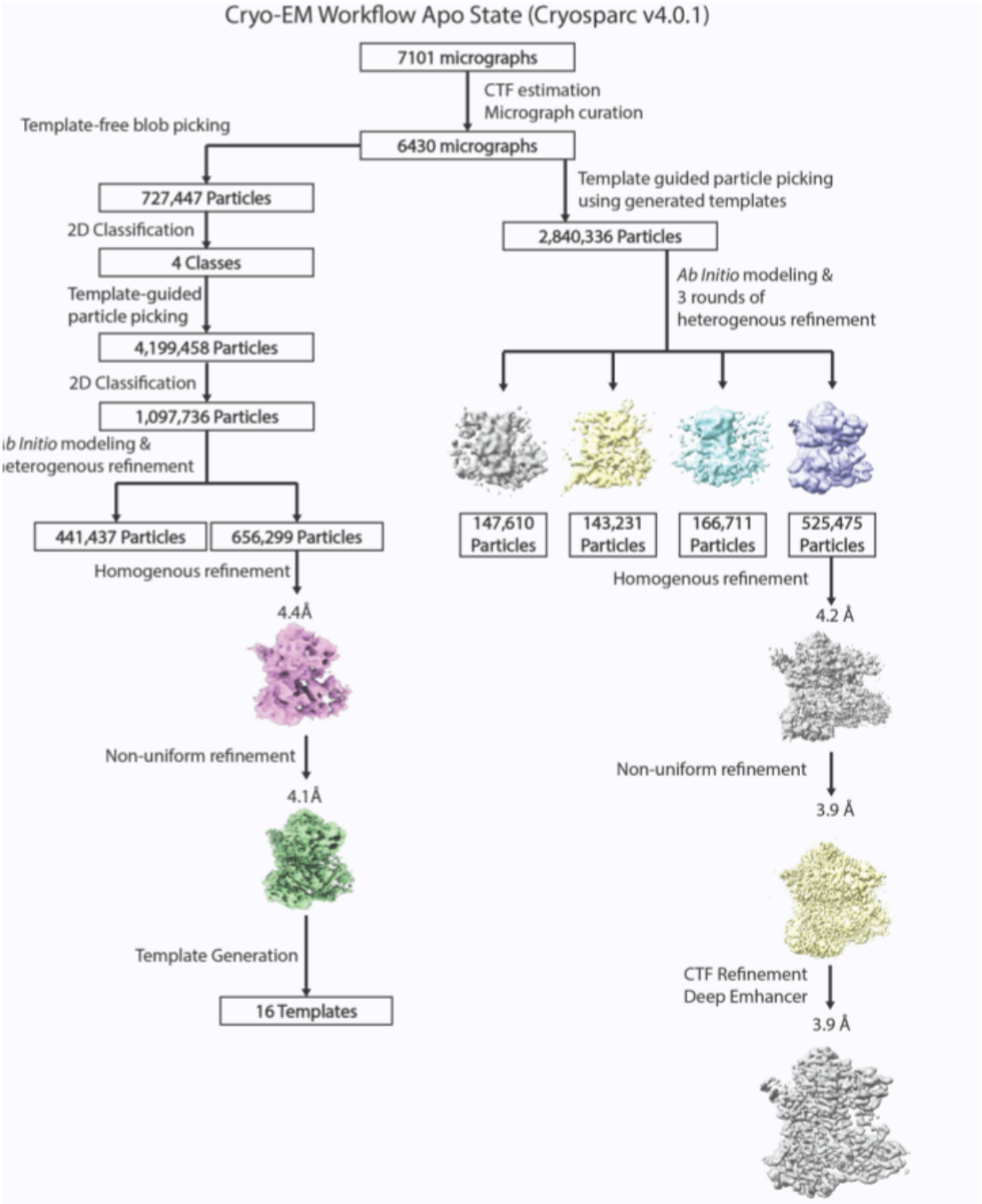

Figure 2.5 Cryo-EM workflow for resolving the structure of apo Arp2/3 complex
Schematic workflow for the image processing done to reconstruct apo Arp2/3 complex. Particle counts are labeled and representative EM density maps are displayed for intermediate steps of the process.

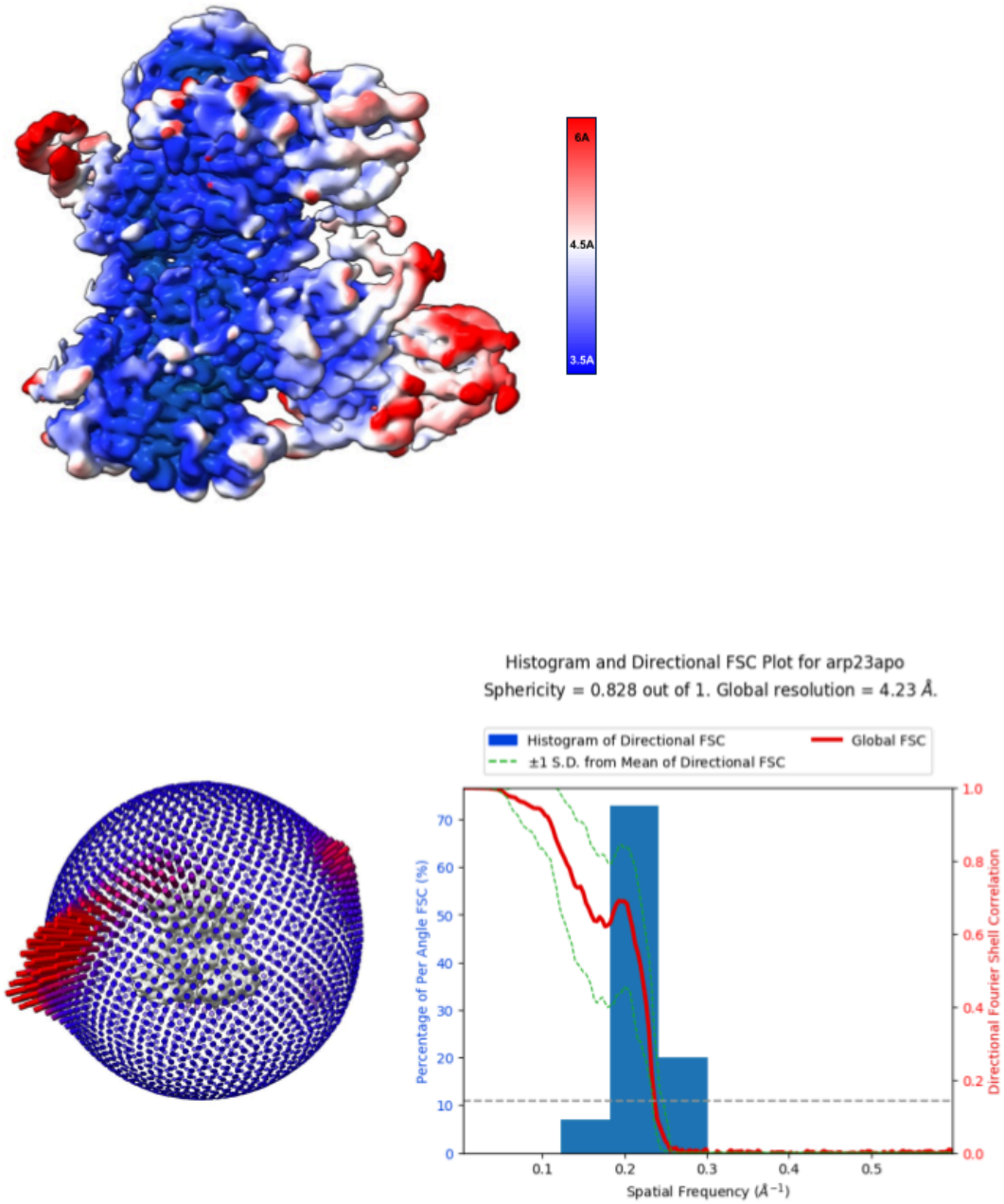

Figure 2.6 Local resolution map and map quality for Arp2/3 with DNA
(Top) Local resolution map of apo Arp2/3 complex. Color key provided. (Bottom Left) Angular distribution representation of structure. (Bottom Right) 3DFSC histogram of structure with a global resolution of 4.23 Å.

Methods

Arp2/3-DNA crosslinking and Western Blots DNA-protein UV crosslinking was performed as previously described (Sasstry 1997). Briefly, NHS-Psoralen (Thermo Scientific) was added to DNA oligo and incubated in the dark at room temperature for 30min in Arp2/3 buffer (20 mM Tris pH 7.5, 25 mM KCl, 1 mM MgCl2, 1 mM DTT). Porcine Arp2/3 (Cytoskeleton) was then added to the "dark" reaction and the mixture incubated for 30min at room temperature. Samples were irradiated with a UV crosslinker (Spectrolinker XL-1000) by placing samples on ice 5cm away from UV light source and irradiating for 60min. Control samples were treated identically except that the preincubation with psoralen was omitted. Western blotting was done with the LiCOR Odyssey to visualize shifts from DNA binding using the following antibodies: rb polyclonal anti-ARPC2 (LSBio, LS-C102803; dilution 1:1000), rb polyclonal anti-ARPC4 (LSBio, LS-C134953; dilution 1:1000), rb polyclonal anti-ARPC5 (Novus Bio, NBP2-14878; dilution 1:1000), ms monoclonal anti-Arp3 (Santa Cruz, sc-48344; dilution 1:1000), ms monoclonal anti-Arp2 (Santa Cruz, sc-166103; dilution 1:1000), ms monoclonal anti-ARPC3 (Santa Cruz, sc-166630; dilution 1:1000), ms monoclonal anti-ARPC1 (Santa Cruz, sc-271342; dilution 1:1000). To detect ARPC1 isoforms, the following antibodies were used as previously described (Kahr et al. Nat Comms 2017): rb polyclonal anti-ARPC1A (Sigma-Aldrich, HPA004334; dilutions 1:1000), and rb polyclonal anti-ARPC1B (Sigma-Aldrich, HPA006550; dilution 1:1000). LiCOR secondaries were as follow: IRDye 680RD Goat anti-Rabbit IgG (LiCOr, 926-68071; dilution 1:10,000) and IRDye 800CW Goat anti-Mouse IgG (LiCOr, 926-32210; dilution 1:10,000).

Cryo-EM sample preparation and data acquisition

Samples of Arp2/3 complex in the apo state were prepared as follows: Acanthamoeba Arp2/3 was diluted to 1uM in vitrification buffer (50mM KCl, 1mM MgCl2, 1mM EGTA, 10mM HEPES ph7, 200uM ATP, 500uM TCEP) and allowed to incubate at room temperature for 30 minutes before vitrification. ssDNA-bound Arp2/3 complex was prepared by diluting Arp2/3 to 0.8uM in vitrification buffer and adding 2uM ssDNA (concentrations were optimized for binding). ssDNA-bound complex was incubated at room temperature for 30 minutes before vitrification.

The same vitrification process was used for both apo state and ssDNA-bound Arp2/3 samples with a Vitrobot: 3ul of sample was applied to freshly glow-discharged 300-Mesh Ultrafoil R1.2/1.3 holey AU grids (Quantifoil). Grids were subsequently blotted with Whatman 41 filter paper for 1 second before being plunged frozen in liquid ethane.

Apo state cryo-EM movies were automatically acquired using SerialEM on a Titan Krios G2 microscope at 300keV equipped with a post-column energy filter and K3 electron detector (Gatan). Images were taken at a nominal magnification of 105,000x in counting mode resulting in a pixel size of 0.835Å. The exposure was 2s with 80 frames and a dose rate of 16e-/pix/s resulting in a nominal dose of 45.8e-/A2. A total of 7,101 micrographs were collected this way at a defocus range of -0.5 to -1.5um for the apo state (Extended Data Figure Aa.).

For the ssDNA-bound structure, cryo-EM movies were automatically acquired using SerialEM on a Talos Arctica at 200keV equipped with a K3 electron detector (Gatan). Images were taken at a nominal magnification of 45,000x in counting mode resulting in a pixel size of 0.865Å. The exposure was 3s with 75 frames and a dose rate of 16e-/pix/s resulting in a nominal

dose of 64.1e-/Å2. A total of 5,032 micrographs were collected this way at a defocus range of -1.0 to -2.0um for the apo state (Extended Data Figure Ab.).

Cryo-EM data processing

All acquired movies were motion-corrected using MotionCorr2. Motion-corrected datasets were imported and processed in cryoSPARC v4.0.2. Contrast transfer function (CTF) estimation was performed using cryoSPARC Patch CTF Estimation.

For the apo state Arp2/3 complex, micrographs below 8Å maximum resolution fit were kept for further processing resulting in 6,430 micrographs. CryoSPARC template-free blob picking, extraction, and 2D classification yielded particle classes to be used for template-based particle picking. All particles during data processing were extracted using a square box size of 360 pixels and unbinned. Template-based particle picking yielded a total of 1,097,736 Arp2/3 particles in the apo state after 2D classification. These particles were used for ab-initio 3D model generation and subsequent rounds of 3D heterogenous refinement which resulted in a particle yield of 656,299. Homogeneous refinement resulted in a 4.4Å global resolution electron density map of apo Arp2/3. Low resolution and preferred orientation artifacts in this reconstruction led us to use this model for 2D template generation and subsequent template-based picking. After another round of particle extraction, 2D classification, ab-initio 3D model generation, and 3D refinement, we generated a 4.1Å global resolution map of apo state Arp2/3 with 256,403 particles. We noted low resolution of subunits ArpC3 and Arp3, possibly due to flexibility of the complex. To improve the resolution of our predicted DNA-binding region we generated a subvolume mask in UCSF ChimeraX and performed local refinement in cryoSPARC. Local refinement produced a map of our apo state Arp2/3 complex at 3.8Å global resolution. This

masked and locally refined map of the Arp2/3 complex consists of ArpC1, ArpC2, ArpC4, ArpC5, and Arp2.

For the ssDNA-bound Arp2/3 complex, micrographs were curated for being under 8Å maximum resolution fit, resulting in 4,082 micrographs. Generated templates from the apo state workflow were used for template-guided particle picking for this +ssDNA dataset resulting in 1,677,776 particles. Two rounds of 2D classification isolated 502,170 particles of the dataset which contained the protein. Ab initio modeling and subsequent heterogenous refinement using two classes, followed by homogenous refinement of the class representing Arp2/3 complex produced a 4.0Å map with 445,505 particles. Local refinement with a mask generated in ChimeraX produced a map at 3.9Å. This locally refined map of ssDNA-bound Arp2/3 complex contains the DNA density, ArpC1, ArpC2, ArpC4, ArpC5, and Arp2. Three rounds of heterogeneous refinement with four classes was then attempted to improve our resolution. The resulting 272,163 particles were used for homogenous refinement and local refinement, but could only result in a resolution of 4.1Å.

Model Building

Model building of the full A. castellani Arp2/3 complex was not attempted due to the current lack of amino acid sequences for the majority of A. castellani Arp2/3 subunits. While the sequence of A. castellani Arp2 protein was available from transcriptomics, the sequence of ArpC1 we could find was inferred from homology. Preliminary modeling was performed for the purposes of identifying potential dna-interacting residues. Alphafold and homology modeling was used to generate an initial backbone from uniprot sequences (UniProt ID: L8GH55 & P53487), which was then rigid-body fitted into our models and iteratively refined using Phenix and Coot.

References

Banitt, I., & Wolfson, H. J. (2011). ParaDock: a flexible non-specific DNA--rigid protein docking algorithm. Nucleic acids research, 39(20), e135.

Belin, B. J., Lee, T., & Mullins, R. D. (2015). DNA damage induces nuclear actin filament assembly by Formin -2 and Spire-½ that promotes efficient DNA repair. [corrected]. eLife, 4, e07735.

Bohnsack, M. T., Stuven, T., Kuhn, C., Cordes, V. C., and Gorlich, D. (2006). A selective block of nuclear actin export stabilizes the giant nuclei of Xenopus oocytes. Nat Cell Biol 8(3), 257-63.

Caridi, C.P., D'Agostino, C., Ryu, T., Zapotoczny, G., Delabaere, L., Li, X., Khodaverdian, V. Y., Amaral, N., Lin, E., Rau, A. R., and Chiolo, I. (2018). Nuclear F-actin and myosins drive relocalization of heterochromatic breaks. Nature 559(7712), 54-60.

Graham, K., Chandrasekaran, A., Wang, L., Ladak, A., Lafer, E. M., Rangamani, P., & Stachowiak, J. C. (2023). Liquid-like VASP condensates drive actin polymerization and dynamic bundling. Nature physics, 19(4), 574–585.

Hatano, S., and Oosawa, F. (1966). Isolation and characterization of plasmodium actin. Biochim Biophys Act 127(2), 488-98.

Hinze, C., and Boucrot, E. (2018). Local actin polymerization during endocytic carrier formation. Biochem Soc Trans 46(3), 565-576.

Pollard, T. D., Blanchoin, L., and Mullins, R. D. (2000). Molecular mechanisms controlling actin filament dynamics in nonmuscle cells. Annu Rev Biophys Biomol Struct 29, 545-76.

Pollard, T. D., and Borisy, G. G. (2003). Cellular motility driven by assembly and disassembly of actin filaments. Cell 112, 453-465.

Schrank, B. R., Aparicio, T., Li, Y., Chang, W., Chait, B. T., Gundersen, G. G., Gottesman, M. E., and Gautier, J. (2018). Nuclear Arp2/3 drives DNA break clustering for homology-directed repair. Nature 559(7712), 61-66.

Zhou, F. Y., Ashton, M., Jiang, Y., Arora, N., Clark, K., Fitzpatrick, K. B., & Haber, J. E. (2025). Arp2/3 and type-I myosins control chromosome mobility and end-resection at double-strand breaks in S. cerevisiae. Nature communications, 16(1), 7212. https://doi.org/10.1038/s41467-025-62377-7

Chapter 3: Electron-Microscopy of Cytoskeletal Proteins from Non-Eukaryotes

Introduction

Nearly all living cells must navigate challenges like maintaining internal organization, motility, and division. To address these challenges, cells utilize a variety of structural proteins which can reversibly polymerize and assemble into micrometer-scale networks as well as generate force. Actins and tubulins are among the most well-conserved structural proteins with homologs found in every domain of life (Wickstead et al., 2011).

The eukaryotic actin filament can be described as a two-start polymer which assembles in an ATP hydrolysis-dependent fashion (Millman et al., 1967; Huxley, 1973). Unlike microtubules, actin filaments do not experience dynamic instability where filaments are subject to occasional "catastrophes" or periods of rapid depolymerization (Mitchison & Kirschner, 1984). Monomers of actin are 42kDa and among virtually all eukaryotes the sequence identity of actin is above 80% (Muller et al., 2005). Actin belongs to a superfamily of proteins which share a similar "actin-like", or hexokinase-like, fold, and bacterial cousins in this family are referred to as Actin-Like Proteins (ALP). Some bacterial ALPs have been found to serve similar cytoskeletal functions like separating plasmids, controlling cell shape, and cytokinesis (Jensen and Gerdes, 1997; Lindås et al., 2008; Ricard and Hirota, 1973). It is hypothesized that the Last Universal Common Ancestor possessed such an ALP considering their existence among all domains of life (it is uncertain if this ancestral ALP could polymerize). Although sharing this commonality, bacterial ALP filaments possess profoundly divergent properties when compared to eukaryotic actin, such as an opposite handed twist of the helix (Galkin et al. 2009), dynamic instability (Garner et al., 2004), or a complete beta barrel. Our lab has recently characterized the divergent dynamics of Alp7A, an ALP that is found in Bacillus subtilis and functions as a plasmid

segregator not dissimilar to a mitotic spindle (Derman et al., 2009). Unlike mammalian actins, Alp7A can undergo dynamic instability when expressed with genes from their operon.

The closest related non-eukaryotic actins would be found in archaea. Genome sequencing of Crenarchea revealed ALPs which shared an approximate 20% sequence identity with eukaryotic actin (Ettema et al., 2011). Although their biological function is still not well understood, further in vitro structural studies revealed these "crenactins" as being capable of polymerizing in a fashion extremely similar to actin: a two-start helix with a right-handed turn (Izoré et al., 2014). Another fascinating example in the literature comes from the Asgard archaea, which possesses so many eukaryotic signature proteins it is hypothesized that these archaea were the engulfing host cell during the eukaryogenesis event. In strong support of this idea, purified gelsolin and profilin-like Asgard archaea proteins are capable of binding mammalian actin and regulating its function (Akıl & Robinson, 2018; Akıl et al., 2022);. Our lab has recently been interested in studying the cytoskeletons of extremophile archaea such as Thermoplasma acidophilum. A crystal structure of TA0583, an actin homolog in this organism which we've dubbed thermoplasmactin, revealed a fold virtually identical to other ALPs (Roeben et al., 2006), but as of current there has not been a reported structure of the filament. Another archaea called Sulfolobus acidocaldarius (Saci) possesses a non-actin-like chromosome segregation cassette called SegA/B (Kalliomaa-Sanford et al., 2012). Work from our lab visualized SegA/B partitioning of chromatin in live cells during division (Charles-Orzsag et al., 2025). SegA appears to form a filamentous bridge not dissimilar to a mitotic spindle in between sister chromatids while SegB localizes to the cell poles. SegA is a small 24.3kDa protein which readily forms dimers and can bind DNA non-specifically (Yen et al., 2021), but there is so far no reported structure of a larger-order polymer.

In this chapter, I present my endeavors to elucidate the structures of several filamentous proteins from non-eukaryotic organisms: Alp7A from Bacillus subtilis, SegA from Sulfolobus acidocaldarius, and TA0583 from Thermoplasma acidophilum.

Results

Straight Alp7A Filaments Tightly Pack into Sheets in an Anti-Parallel Orientation

In alignment with our lab's prior unpublished observations, filaments of Alp7A prepared on EM grids heavily preferred to bundle into flat sheets of heterogeneous width that may occasionally twist or kink over long length scales (Figure 3.1). Higher concentrations of salt up to 1M were known to disrupt this bundling behavior, but in our experiments these higher salt regimes would severely decrease the amount of protein that stayed on carbon grids. Looking closer at these bundles through 2D Classification, we observed that each filament appears to pack in an anti-parallel fashion with its neighbor. In addition, the filaments within these bundles appeared straight and did not have a helical twist nearly as extreme as actin (Figure 3.1). As a result each monomer along the length of a filament is participating in inter-filament contacts as opposed to periodic contacts limited by twist. Because of Alp7A's consistent bundling and preferred sheet orientation, it was untenable to produce a 3D reconstruction of the single Alp7A filament, although we were able to generate a single high quality 2D class average of sparse single filaments which displayed severe orientation bias (likely because they protrude from 2D sheets and combined with the lack of twist would only show one face). The crystal packing of a previously solved x-ray crystallographic structure (PDB: 5EC0) was also not informative for the filament/bundling architecture. Instead, we used Alfafold3 to predict a multimeric structure of Alp7A with five copies of the monomer, and simulated 2D projections of the predicted filament to compare with our experimental data. Astonishingly, the filament predicted by Alfafold generated nearly identical 2D projections when compared to our 2D class averages, which suggested that our Alfafold-predicted filament closely approximates the architecture of the Alp7A helix (Figure 3.1). Based on the predicted model, Alp7A polymerizes as a two-start

filament with a near-imperceptible helical twist (although we cannot verify its true twist without an experimental structure). Because of this tighter filament packing, this predicted structure of Alp7A has a greater amount of inter-monomer buried surface area when compared to rabbit actin and a close prokaryotic cousin ParM. Analysis of the electrostatics on this predicted model contextualized with the packing of the filament in our experimental class averages suggest that several clustered acidic residues found along a protruding edge of the incorporated monomer could be responsible for inter-filament interactions: Asp193 ,Glu195, Asp196, Asp198, Glu201, Glu353, and Asp350 (Figure 3.1).

SegA Forms Microtubule-Like Filaments on Grids

Our initial work in determining the structure of the components of the SegA/B/S system began with trying to reconstitute complexes of these proteins bound to DNA. While biochemical validations suggested that the proteins were forming higher order polymers, we were unable to visualize any complexes on ice. This is perhaps due to the flexibility of the DNA and lack of stabilizing interactions between protein components (invoking imagery of flexible beads on a string instead of a compacted complex). Even if dimers of SegA/B were forming, their molecular weight (approx. 50kDa) would still be on the untenable end for cryo-EM reconstruction. After changing our purification protocol and using increased concentrations of SegA (upwards of 50uM), we began to observe what appeared to be short, flexible filaments and the occasional appearance of large, presumably hollow tubules (short filaments appear in 1/3 of micrographs, tubules in 1/100 of micrographs)(Figure 3.2). These filaments were present regardless of the addition of DNA. Based on 2D class averages of the sparse tubules we could collect, these large tubes had a diameter comparable to FtsZ and microtubules (around 250A). These large SegA filaments also bore a distinct checkerboard-like pattern which was easy to resolve with only tens

of particles, suggesting an ordered helical symmetry. We postulate that the monomers of SegA first assemble into flexible protofilaments one or two monomers thick before assembling laterally to form large tubules (Figure 3.2).

Thermoplasmactin Forms a Left-Handed Double Helix which can Bundle into Triplets

Negative stain micrographs show thermoplasmactin forms heavily bundled, disordered clusters in the presence of ATP and low salt, but with plentiful populations of single filaments that were amenable for helical refinement (Figure 3.3). When frozen on grids, we saw far less bundling and, similar to Alp7A, a reduced presence of protein in higher salt concentrations. Notably, the bundles that could be seen appeared to be parallel doublets of filaments, and the majority of filaments on ice were found in these doublets. We were able to collect sufficient data on single thermoplasmactin filaments to helically reconstruct its structure to 3.3A resolution (Figures 3.3B-C, 3.5)(Table 3). The single filament is a left-handed two-start helix with a twist of 163.5 degrees, a rise of 25 angstroms, and approximately 2.2 subunits per turn (or ~11 subunits per full face turn of the filament). These helical characteristics and the filament's bundling behavior closely resemble another filament called ParM, a bacterial relative (Bharat et al., 2015; Galkin et al., 2009)(Figure3.3B-C). We then used particles of the bundled filament to perform single particle refinement and arrived at a low-resolution structure of the bundle. To our surprise, this bundle was a triplet, not a doublet, of filaments (Figure 3.4). Fascinatingly, each filament in the triplet was oriented identically and therefore at any given cross-section of the bundle the filament faces would appear parallel to one another (Figure 3.4). By inspecting the orientations of the prominent beta barrels, we can determine that all filaments in the bundle are parallel i.e. their pointed(+) ends are oriented in the same direction, they are also nearly in-register as opposed to offset. Unlike ParM, which forms doublets using face-to-edge interactions(Bharat et

al., 2015), thermoplasmactin formed triplets using edge-to-edge interactions where any two pairs of filaments would interact with one another around intervals of 11 subunits (or an approximate full turn of a helix) and about half as many subunits (or a half turn)(Figure3.4B-C),. Due to the structure's low resolution, the specific interfilament interaction(s) that enable triple bundles is unclear. The filaments in this triplet also appear to be subtly supercoiled around the central axis of the bundle to accommodate these interactions.

Discussion

Cytoskeletons are one of the most well-conserved structures that can be found across all domains of life. Studying non-eukaryotic cytoskeletons is important for understanding the emergence of this structure in evolutionary time and how ancient cells co-opted available proteins to perform structural functions. In this chapter, we presented our efforts in understanding the structures of several filamentous proteins in non-eukaryotic organisms. We discovered that Alp7A forms straight, low-twist filaments which tightly pack into sheets and using Alfafold we approximated the structure of these filaments. After difficulty in reconstituting any SegA complexes on ice, we generated the first evidence of SegA's filament architecture as a microtubule-like structure. Our most successful endeavor in this foray is determining the high-resolution structure of TA0583 or thermoplasmactin, which forms a ParM-like helix and can bundle into parallel triplets.

The SegA/B system has been a subject of rigorous cell biological study for our lab. In beautifully performed hot microscopy experiments, SegA was found to form mitotic spindle-like bridges between sister chromatids during cell division (Charles-Orzsag, 2025). We believe the tubules observed in EM are an important component of this separation machinery. During cell division, SegA localizes near the center of the cell at the division plane before elongating into a bipolar structure which also pushes the sister chromatins (anchored with SegB) to the cell poles. It is possible that the tubule structures we have visualized with EM in this study are the primary force-generating filament which drives Saci's chromosome segregation. It is nearly certain that optimizing the biochemistry of tube formation and further cryo-EM data collection would yield a high resolution structure of the tube given its helical symmetry visible in 2D class averages.

In our study, two of these proteins belong to the actin-like superfamily where members possess the classic actin/hexokinase fold: Alp7A and thermoplasmactin. At a glance, these two proteins do closely resemble each other with each bearing an overall "heart shaped" architecture bisected by a hinge region (typical of actins) complete with a beta barrel as one lobe of the heart. But assembled as polymers, Alp7A and thermoplasmactin adopt strongly divergent morphologies. Alp7A maintains low-twist helixes that bury more surface area than related ALPs. These straight filaments then associate laterally to form flat sheets with an indeterminate limit for incorporated filaments. It is uncertain how Alp7A's sheet-forming behavior contributes to its function. Alp7R is another protein expressed on the same operon as Alp7A, and is critical for regulation of Alp7A's expression and promoting dynamic instability in Alp7A filaments. In B. subtilis cells the knockout of Alp7R causes overexpression of Alp7A which forms thick, static filaments in the cytoplasm (Derman et al., 2012). Because Alp7A sheets are formed by alternating anti-parallel filaments, it is difficult to conceive of these sheets as being the dynamic filaments which participate in plasmid segregation. Instead we can speculate that these sheets function as an inert non-force-generating reservoir of Alp7A. In unpublished findings, the presence of Alp7R also promoted single filaments in negative stain, substantiating the idea that the sheet is not the primary filament driving plasmid separation in bacteria. Further structural work to identify how Alp7R interacts with Alp7A filaments or sheets will be critical for understanding how dynamism is achieved by the filament. In addition, future studies can focus on mutagenesis of the acidic residues that appear important for inter-filament interaction to generate a non-bundling Alp7A mutant for the purposes of single filament reconstruction.

thermoplasmactin adopts a helix that is reminiscent of ParM and bundles as a parallel, virtually in-register triplet with each filament contacting each other periodically. As of current,

thermoplasmactin's biological function is completely unclear, although it is speculated to be important in a capacity similar to other cytoskeletons due to homology with ParM and actins as well as its ability to form bundles of filaments in vitro (Hara et al., 2007). This triplet structure presents an intriguing geometry question: To what degree do the filaments need to supercoil and how subtle of a lengthwise offset per filament is sufficient to allow for stable interfilament contact formation over long length scales? These questions will motivate the bulk of future efforts to study this protein both using further EM techniques to improve the structure and mathematical modeling.

Table 3.1 Cryo-EM data collection, refinement, and validation statistics for ALP

	thermoplasmactin Filament	thermoplasmactin Bundle
Data collection and processing		
Magnification	105,000	105,000
Voltage (kV)	300	300
Electron Exposure (e-/A^2)	47.7	47.7
Defocus Range (μM)	-0.5-1.5	-0.5-1.5
Pixel Size (Å)	0.8189	0.8189
Initial Micrographs	3,139	
Final Particle Count	26,670	23,209
Map Resolution (FSC threshold 0.143)	3.33	4.67
Refinement (Phenix)		
Initial Model Used	AF-Q9HKL4	
Model Resolution (FSC threshold 0.5)	3.8	
Map CC (Volume)	0.86	
B Factor ($Å^2$)	11.9	
Validation		
MolProbity Score	1.71	
All-Atom Clashscore	4.42	
Rotamer Outliers	0.00	
C-Beta Outliers	0.00	
Ramachandran Plot		
Favored (%)	95.58	
Allowed (%)	4.42	
Outliers (%)	0.00	

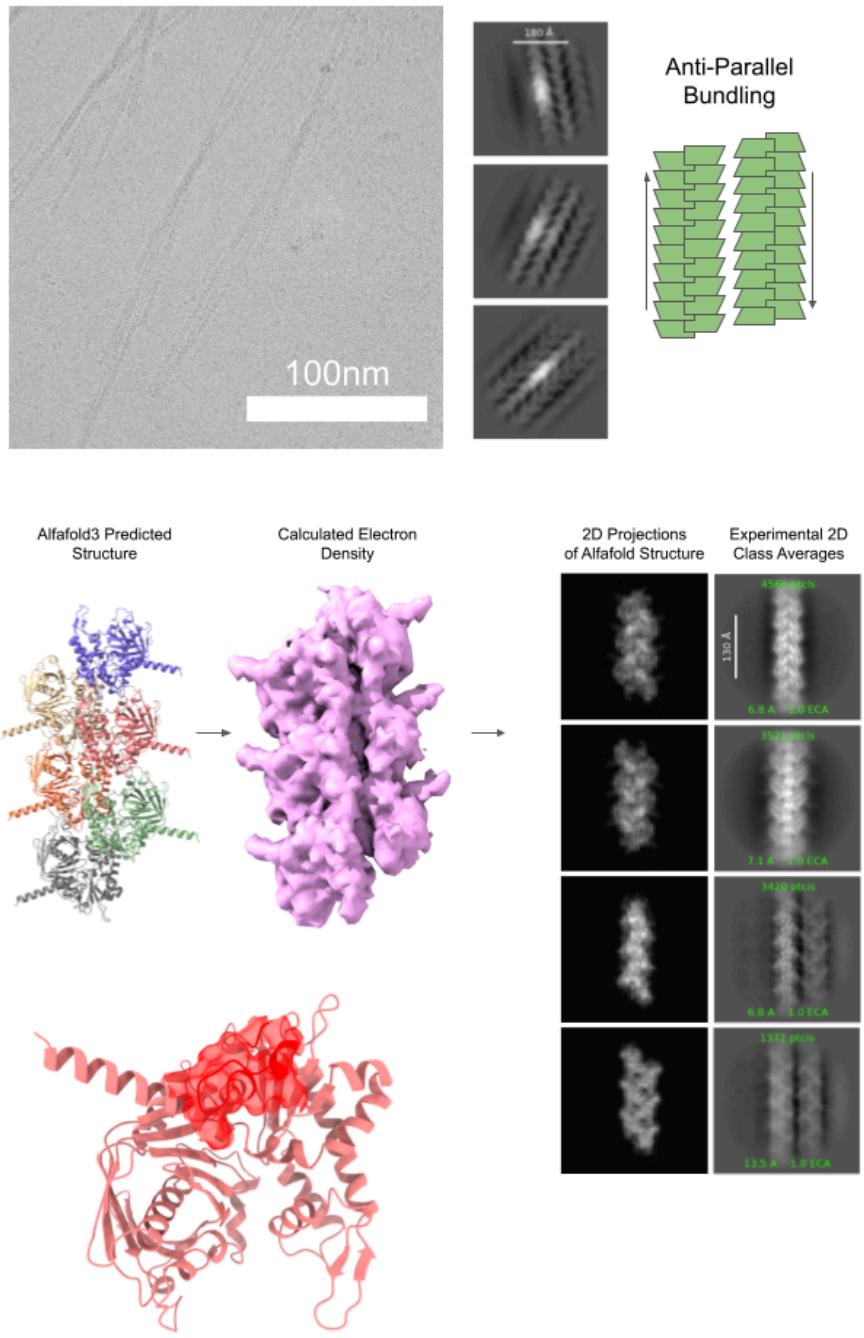

Figure 3.1 Alp7A filaments form anti-parallel bundles which contact each other on the broad face of each monomer

(Top Left) Representative micrograph of Alp7A bundles observed on Lacey Carbon grids. (Top Right) 2D Class averages of segments of the bundles and model of anti-parallel bundle interaction. (Middle) The Alfafold3-generated model (multicolored) of the Alp7A had its electron density calculated (pink) and 2D projections of this density were generated with high similarity to experimental data. (Bottom) Model display of the negatively-charged patch of residues (red transparent surface) on a ridge of Alp7A which may be explanatory for its bundling behavior.

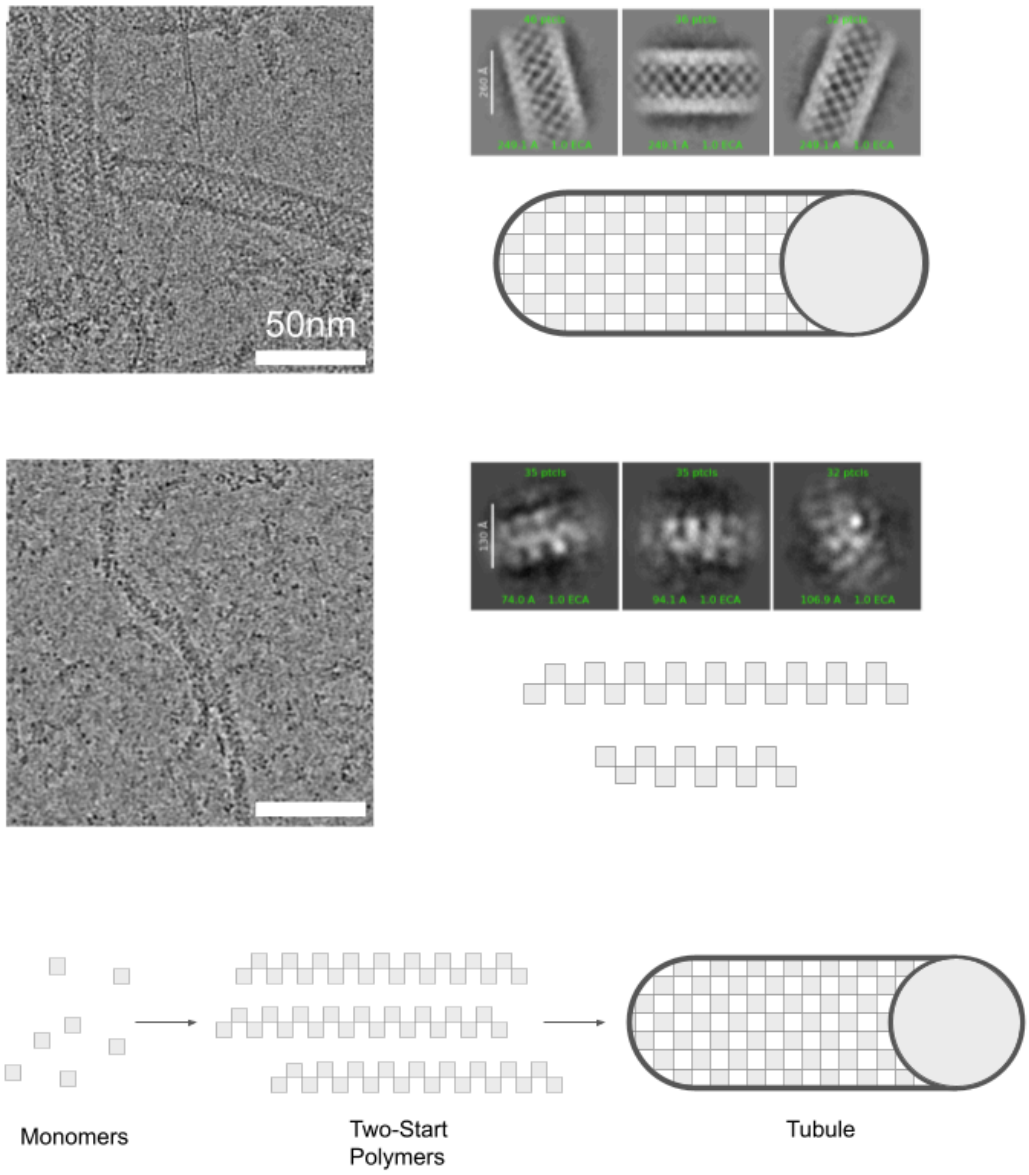

Figure 3.2 SegA forms large tubules and two-start polymers in vitro without DNA or SegB
(Top) Representative micrograph image of the SegA tubules on Lacey Carbon grids (left) with 2D class averages of tubules and a cartoon depiction of their structure. Tubules are approximately 250 Å in diameter and appeared in 3% of micrographs. (Middle) Representative micrograph image of SegA "protofilaments" (left) with related 2D class averages and cartoon depiction of an alternating of their two-start polymer structure. These polymers were approximately 100 Å in diameter and were found in 14% of micrographs. (Bottom) Model for assembly of the tubule: monomers first form the two-start protofilament and protofilaments laterally associate to form tubes.

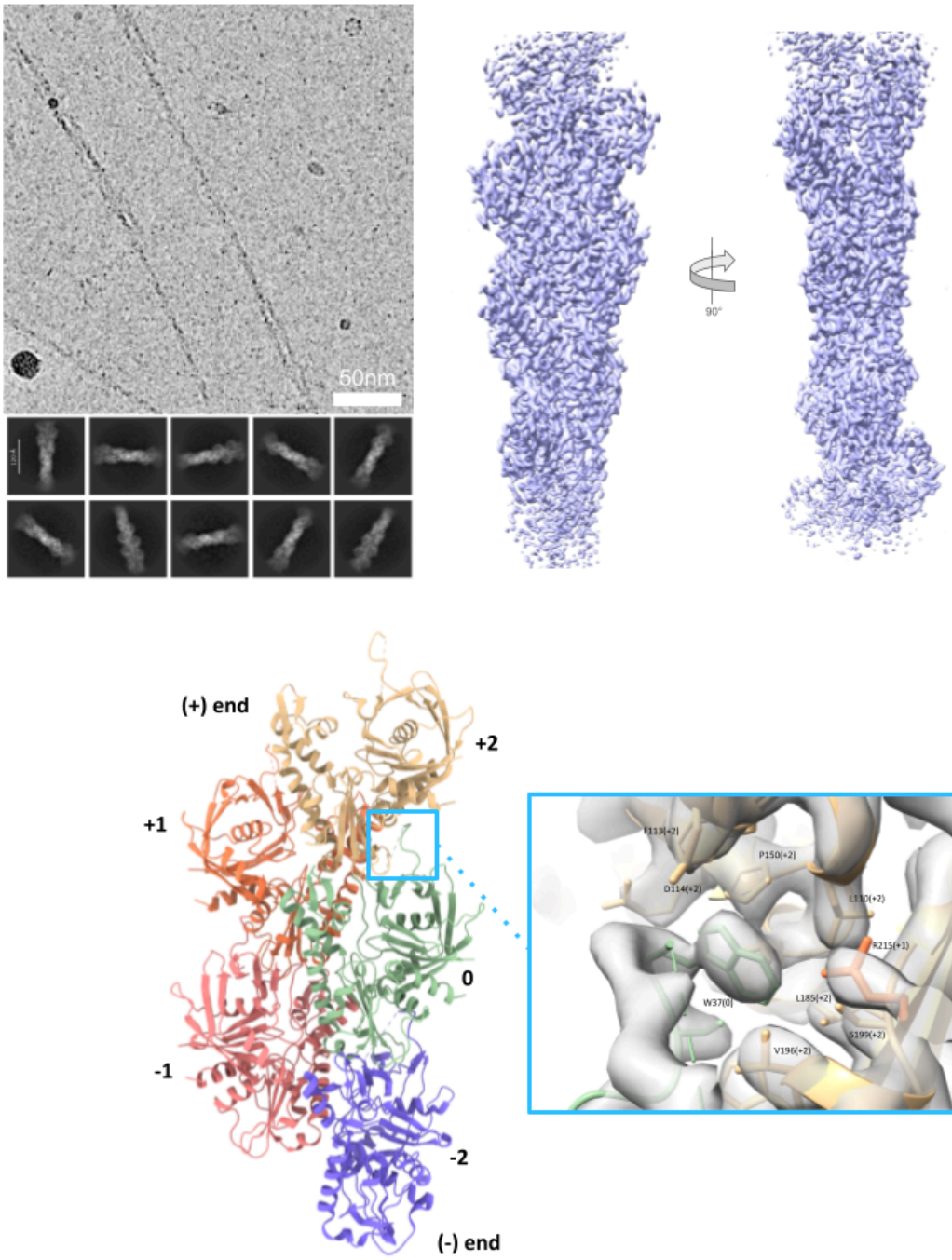

Figure 3.3 Thermoplasmactin forms ParM-like two-start filaments
(Top Left) Representative micrograph image of thermoplasmactin filaments which exist as single polymers or bundles. Bottom: 2D class averages of single thermoplasmactin filaments. (Top Right) EM density map of thermoplasmactin single filament (light purple). The polymer can be described as a two-start helix with a twist of 163.5 degrees and rise of 25 Å which is similar to ParM, a bacterial cousin. (Bottom left) Multicolored model of thermoplasmactin filament with polar ends labeled and monomers labeled relative to central monomer (which is making every possible intermonomer contact). (figure caption continued on the next page)

(figure caption continued from the last page) Blue-outlined box is a close-up view of the D-Loop of the central filament, which uses a tryptophan to engage in hydrophobic contacts with two other monomers of the protofilament (one lateral, one longitudinal).

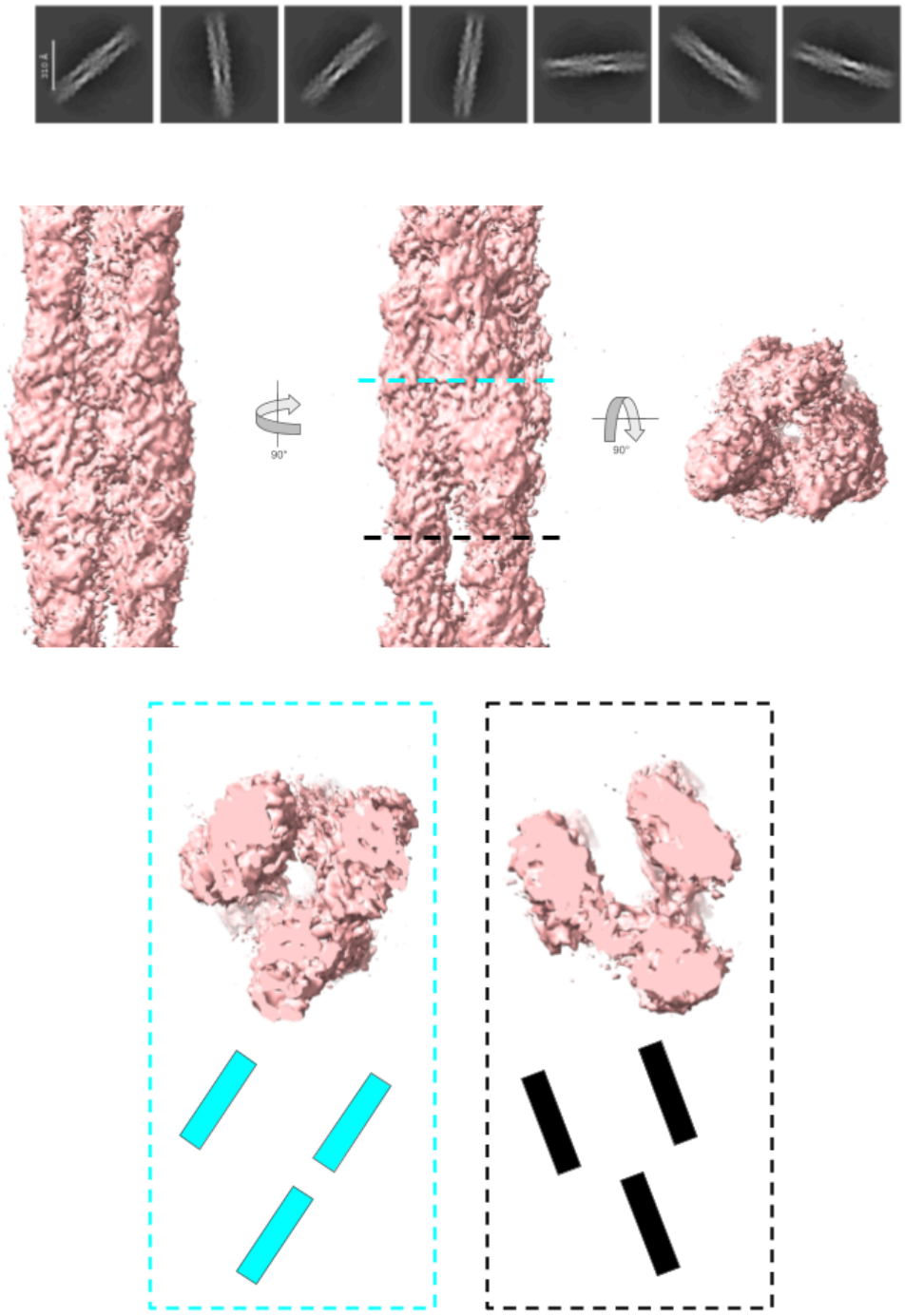

Figure 3.4 Triplet bundles of thermoplasmactin are made of parallel and in-register filaments
(Top) 2D class averages of the thermoplasmactin triplet bundle. (Middle) EM density map of thermoplasmactin triplet from various viewing angles. (figure caption continued on the next page)

(figure caption continued from the last page) The bundle is composed of parallel filaments which gently corkscrew around the central axis of the bundle. Each filament is additionally about in-register with one-another which can be observed in cross sections (Bottom, blue and black outlined). Side-to-side interfilament contacts periodically arise within the triplet.

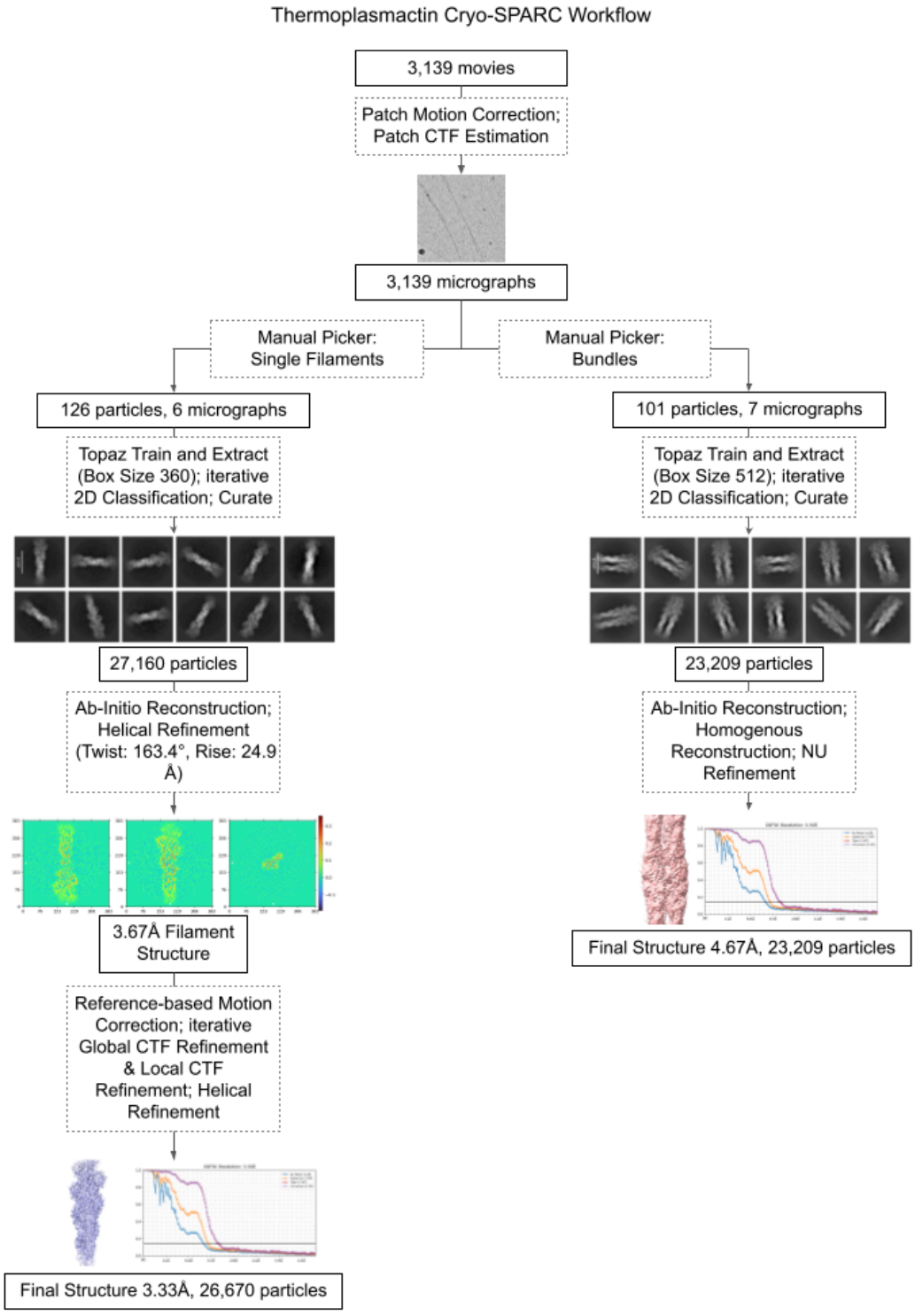

Figure 3.5 Cryo-EM workflow for the thermoplasmactin filament and bundle structure
Schematic workflow for the image processing done to reconstruct both the single filament and bundled triplet of thermoplasmactin. Particle counts are labeled and representative EM density maps are displayed for intermediate steps of the process. Both structures were reconstructed from the same dataset where both single filament and bundle particles could be extracted.

Methods

Cryo-EM Screening and Data Collection

Samples of Alp7A and SegA were polymerized to equilibrium. 300 Mesh Lacey Carbon on AU grids were glow discharged with a plasma cleaner. Vitrification was done using a Vitrobot, 3ul of sample was applied to grids and made to incubate for 15 seconds at room temperature before a 1 second blot using Whatman number 1 filter paper, followed by plunge freezing in liquid ethane. Grids were screened and data was collected using an on-site Talos Arctica at 200keV equipped with a K3 detector (Gatan). Using SerialEM, micrographs were captured at a magnification of 45,000x in counting mode resulting in a pixel size of 0.865Å. Each exposure was 75 frames and a dose rate of 16e-/pix/s resulting in a nominal dose of 64.1e-/Å2. Data was collected at a defocus range of -1.0 to -2.0 um. 9,455 micrographs were collected this way for Alp7A, and 1,462 micrographs were collected for SegA.

Samples of thermoplasmactin were polymerized to equilibrium. 300 Mesh Lacey Carbon on AU grids were glow discharged with a plasma cleaner. Vitrification was done using a Vitrobot, 3ul of sample was applied to grids and made to incubate for 15 seconds at room temperature before a 1 second blot using Whatman number 1 filter paper, followed by plunge freezing in liquid ethane. Cryo-EM movies of this sample were automatically acquired using SerialEM on a Titan Krios G2 microscope at 300keV equipped with a post-column energy filter and K3 electron detector (Gatan). Images were taken at a nominal magnification of 105,000x in counting mode resulting in a pixel size of 0.8189Å. The exposure was 2s with 80 frames and a dose rate of 16e-/pix/s resulting in a nominal dose of 47.7e-/A2. A total of 3,139 movies were collected this way at a defocus range of -0.5 to -1.5um.

CryoEM Data Processing

All acquired movies were motion-corrected using MotionCorr2. Motion-corrected datasets were imported and processed in cryoSPARC v4.0.2. Contrast transfer function (CTF) estimation was performed using cryoSPARC Patch CTF Estimation.

Preliminary data for Alp7A and SegA were generated using the general workflows for single particle analysis in cryoSPARC (filament tracer, extraction, 2D classification). 2D projections of the Alp7A Alfafold3 model were made using the "Create Templates" job in cryoSPARC with a ChimeraX-calculated electron density map as input.

For thermoplasmactin, manually picked segments of single (126 particles) and bundled (101 particles) filaments were used to train separate Topaz learning models using the cryoSPARC wrapper. After Topaz extraction, both sets of particles were put through iterative 2D classification to select groups which averaged classes with high resolution features (single: 27,160 particles; bundle: 23,209 particles). Using ab-initio reconstruction, homogenous refinement, and NU-refinement; the triplet bundle structure was resolved to a global resolution of 4.67 Å (although several features resolved far lower). An initial ab-initio structure of the single thermoplasmactin filament was used to empirically derive the helical parameters of the filament using cryoSPARC's Symmetry Search utility. An initial helical structure using these parameters resolved to a global resolution of 3.67 Å which was then used for iterative Reference-Based Motion Correction and CTF Refinement. This yielded a final structure of the single thermoplasmactin filament at 3.33 Å global resolution.

Additional specific information for the data collected/processed can be found in Table 1.

Cryo-EM Model Building and Refinement

The model for thermoplasmactin density map was built by starting with an Alphafold predicted structure of the monomer (AF-Q9HKL4). Initial model was rigid-body fit into the EM density map in ChimeraX in a central location for the filament, and poorly resolved portions of the D-Loop were manually deleted before refinement in Phenix.We then performed iterative refinement using Phenix real-space refine with secondary restraints, followed by manual adjustments in Coot. After initial cycles we then removed geometry and reference restraints and improved map-to-model accuracy through further iterative refinement with Phenix and Coot. Once we obtained a satisfactory monomer structure, we modelled five monomers of thermoplasmactin into the filament map using rigid body fitting in order to capture all relevant inter-monomer contacts within the central subunit. A few rounds of refinement and manual adjustment yielded our final thermoplasmactin filament structure. All depictions of cryo-EM density maps and protein structures were prepared using UCSF ChimeraX or UCSF Chimera.

References

Akıl, C., Robinson, R.C. Genomes of Asgard archaea encode profilins that regulate actin. Nature 562, 439–443 (2018).

Akıl, C., Tran, L. T., Orhant-Prioux, M., Baskaran, Y., Senju, Y., Takeda, S., Chotchuang, P., Muengsaen, D., Schulte, A., Manser, E., Blanchoin, L., & Robinson, R. C. (2022). Structural and biochemical evidence for the emergence of a calcium-regulated actin cytoskeleton prior to eukaryogenesis. Communications biology, 5(1), 890.

Bharat, T. A., Murshudov, G. N., Sachse, C., & Löwe, J. (2015). Structures of actin-like ParM filaments show architecture of plasmid-segregating spindles. Nature, 523(7558), 106–110.

Charles-Orszag, A., Lord, S. J., Herrera, N., Strauskulage, L., Bhowmick, A., Goddard, T., Wassmer, B., van Wolferen, M., Asper, G., Flis, A., Rodriguez, J., Redding, S., Rosenberg, O., Albers, S. V., & Mullins, R. D. (2025). Archaeal SegAB forms a bipolar structure that promotes chromosome segregation in spherical cells. bioRxiv : the preprint server for biology, 2025.04.15.649018.

Derman, A. I., Becker, E. C., Truong, B. D., Fujioka, A., Tucey, T. M., Erb, M. L., Patterson, P. C., & Pogliano, J. (2009). Phylogenetic analysis identifies many uncharacterized actin-like proteins (Alps) in bacteria: regulated polymerization, dynamic instability and treadmilling in Alp7A. Molecular microbiology, 73(4), 534–552.

Derman, A. I., Nonejuie, P., Michel, B. C., Truong, B. D., Fujioka, A., Erb, M. L., & Pogliano, J. (2012). Alp7R regulates expression of the actin-like protein Alp7A in Bacillus subtilis. Journal of bacteriology, 194(10), 2715–2724.

Ettema, T. J., Lindås, A. C., & Bernander, R. (2011). An actin-based cytoskeleton in archaea. Molecular microbiology, 80(4), 1052–1061.

Galkin, V. E., Orlova, A., Rivera, C., Mullins, R. D., & Egelman, E. H. (2009). Structural polymorphism of the ParM filament and dynamic instability. Structure (London, England : 1993), 17(9), 1253–1264.

Garner, E. C., Campbell, C. S., & Mullins, R. D. (2004). Dynamic instability in a DNA-segregating prokaryotic actin homolog. Science (New York, N.Y.), 306(5698), 1021–1025.

Hara, F., Yamashiro, K., Nemoto, N., Ohta, Y., Yokobori, S., Yasunaga, T., Hisanaga, S., & Yamagishi, A. (2007). An actin homolog of the archaeon Thermoplasma acidophilum that retains the ancient characteristics of eukaryotic actin. Journal of bacteriology, 189(5), 2039–2045.

Izoré, T., Duman, R., Kureisaite-Ciziene, D., & Löwe, J. (2014). Crenactin from Pyrobaculum calidifontis is closely related to actin in structure and forms steep helical filaments. FEBS letters, 588(5), 776–782.

Jensen, R. B., & Gerdes, K. (1997). Partitioning of plasmid R1. The ParM protein exhibits ATPase activity and interacts with the centromere-like ParR-parC complex. Journal of molecular biology, 269(4), 505–513.

Kalliomaa-Sanford, A. K., Rodriguez-Castañeda, F. A., McLeod, B. N., Latorre-Roselló, V., Smith, J. H., Reimann, J., Albers, S. V., & Barillà, D. (2012). Chromosome segregation in Archaea mediated by a hybrid DNA partition machine. Proceedings of the National Academy of Sciences of the United States of America, 109(10), 3754–3759.

Lindås, A. C., Karlsson, E. A., Lindgren, M. T., Ettema, T. J., & Bernander, R. (2008). A unique cell division machinery in the Archaea. Proceedings of the National Academy of Sciences of the United States of America, 105(48), 18942–18946.

Millman, B., Elliott, G. & Lowy, J. Axial Period of Actin Filaments: X-ray Diffraction Studies. Nature 213, 356–358 (1967).

Mitchison, T., & Kirschner, M. (1984). Dynamic instability of microtubule growth. Nature, 312(5991), 237–242.

Muller, J., Oma, Y., Vallar, L., Friederich, E., Poch, O., Winsor, B. (2005). Sequence and comparative genomic analysis of actin-related proteins. Molecular Biology of the Cell, 16(12), 5736-5748.

Hara, F., Yamashiro, K., Nemoto, N., Ohta, Y., Yokobori, S., Yasunaga, T., Hisanaga, S., & Yamagishi, A. (2007). An actin homolog of the archaeon Thermoplasma acidophilum that retains the ancient characteristics of eukaryotic actin. Journal of bacteriology, 189(5), 2039–2045.

Huxley, H.E. (1973). Structural changes in the actin- and myosin-containing filaments during contraction. Cold Spring Harbor Symposia on Quantitative Biology, 37, 361–376.

Ricard, M., & Hirota, Y. (1973). Process of cellular division in Escherichia coli: physiological study on thermosensitive mutants defective in cell division. Journal of bacteriology, 116(1), 314–322.

Roeben, A., Kofler, C., Nagy, I., Nickell, S., Hartl, F. U., & Bracher, A. (2006). Crystal structure of an archaeal actin homolog. Journal of molecular biology, 358(1), 145–156.

Wickstead, B., & Gull, K. (2011). The evolution of the cytoskeleton. The Journal of cell biology, 194(4), 513–525.

Yen, C. Y., Lin, M. G., Chen, B. W., Ng, I. W., Read, N., Kabli, A. F., Wu, C. T., Shen, Y. Y., Chen, C. H., Barillà, D., Sun, Y. J., & Hsiao, C. D. (2021). Chromosome segregation in Archaea: SegA- and SegB-DNA complex structures provide insights into segrosome assembly. Nucleic acids research, 49(22), 13150–13164.

References for cryo-EM tools used

Adams, P. D., Grosse-Kunstleve, R. W., Hung, L. W., Ioerger, T. R., McCoy, A. J., Moriarty, N. W., Read, R. J., Sacchettini, J. C., Sauter, N. K., & Terwilliger, T. C. (2002). PHENIX: building new software for automated crystallographic structure determination. Acta crystallographica. Section D, Biological crystallography, 58(Pt 11), 1948–1954.

Berman, H., Henrick, K., Nakamura, H., & Markley, J. L. (2007). The worldwide Protein Data Bank (wwPDB): ensuring a single, uniform archive of PDB data. Nucleic acids research, 35(Database issue), D301–D303.

Emsley, P., Lohkamp, B., Scott, W. G., & Cowtan, K. (2010). Features and development of Coot. Acta crystallographica. Section D, Biological crystallography, 66(Pt 4), 486–501.

Meng, E. C., Goddard, T. D., Pettersen, E. F., Couch, G. S., Pearson, Z. J., Morris, J. H., & Ferrin, T. E. (2023). UCSF ChimeraX: Tools for structure building and analysis. Protein science : a publication of the Protein Society, 32(11), e4792.

Punjani, A., Rubinstein, J. L., Fleet, D. J., & Brubaker, M. A. (2017). cryoSPARC: algorithms for rapid unsupervised cryo-EM structure determination. Nature methods, 14(3),

Publishing Agreement

It is the policy of the University to encourage open access and broad distribution of all theses, dissertations, and manuscripts. The Graduate Division will facilitate the distribution of UCSF theses, dissertations, and manuscripts to the UCSF Library for open access and distribution. UCSF will make such theses, dissertations, and manuscripts accessible to the public and will take reasonable steps to preserve these works in perpetuity.

I hereby grant the non-exclusive, perpetual right to The Regents of the University of California to reproduce, publicly display, distribute, preserve, and publish copies of my thesis, dissertation, or manuscript in any form or media, now existing or later derived, including access online for teaching, research, and public service purposes.

DocuSigned by:

6E8E81756F5B4C9...

Author Signature

08/17/2026

Date